Journal of Controlled Release 376 (2024) 678–700

Contents lists available at ScienceDirect

Journal of Controlled Release

journal homepage: www.elsevier.com/locate/jconrel

Optimizing lipid nanoparticles for fetal gene delivery in vitro, ex vivo, and aided with machine learning

Amr Abostait [a,b], Mahmoud Abdelkarim [a,c], Zeqing Bao [d], Yuichiro Miyake [e,f], Wai Hei Tse [e], Caterina Di Ciano-Oliveir [a], Tina Buerki-Thurnherr [g], Christine Allen [d], Richard Keijzer [e], Hagar I. Labouta [a,b,c,d,*]

[a] Keenan Research Centre for Biomedical Science, Unity Health Toronto, Toronto M5B 1T8, Canada
[b] College of Pharmacy, University of Manitoba, Winnipeg R3E 0T5, Canada
[c] Biomedical Engineering, Faculty of Engineering, University of Toronto, Toronto M5S 3G9, Canada
[d] Leslie Dan Faculty of Pharmacy, University of Toronto, Toronto, ON M5S 3M2, Canada
[e] Department of Surgery, Division of Pediatric Surgery, Max Rady College of Medicine, Rady Faculty of Health Sciences, University of Manitoba and Children's Hospital Research Institute of Manitoba, Winnipeg, MB R3E 3P4, Canada
[f] Department of Pediatric General and Urogenital Surgery, Juntendo University School of Medicine, 2-1-1 Hongo Bunkyo-ku, Tokyo 113-8421, Japan
[g] Laboratory for Particles-Biology Interactions, Swiss Federal Laboratories for Materials Science and Technology (Empa), St. Gallen 9014, Switzerland

ARTICLE INFO

Keywords:
Lipid nanoparticles
Fetal gene delivery
siRNA
Transplacental transport
Placenta
Machine learning

ABSTRACT

There is a clinical need to develop lipid nanoparticles (LNPs) to deliver congenital therapies to the fetus during pregnancy. The aim of these therapies is to restore normal fetal development and prevent irreversible conditions after birth. As a first step, LNPs need to be optimized for transplacental transport, safety on the placental barrier and fetal organs and transfection efficiency. We developed and characterized a library of LNPs of varying compositions and used machine learning (ML) models to delineate the determinants of LNP size and zeta potential. Utilizing different in vitro placental models with the help of a Random Forest algorithm, we could identify the top features driving percentage LNP transport and kinetics at 24 h, out of a total of 18 input features represented by 41 LNP formulations and 48 different transport experiments. We further evaluated the LNPs for safety, placental cell uptake, transfection efficiency in placental trophoblasts and fetal lung fibroblasts. To ensure the integrity of the LNPs following transplacental transport, we screened LNPs for transport and transfection using a high-throughput integrated transport-transfection in vitro model. Finally, we assessed toxicity of the LNPs in a tracheal occlusion fetal lung explant model. LNPs showed little to no toxicity to fetal and placental cells. Immunoglobin G (IgG) orientation on the surface of LNPs, PEGylated lipids, and ionizable lipids had significant effects on placental transport. The Random Forest algorithm identified the top features driving LNPs placental transport percentage and kinetics. Zeta potential emerged in the top driving features. Building on the ML model results, we developed new LNP formulations to further optimize the transport leading to 622 % increase in transport at 24 h versus control LNP formulation. To induce preferential siRNA transfection of fetal lung, we further optimized cationic lipid percentage and the lipid-to-siRNA ratio. Studying LNPs in an integrated placental and fetal lung fibroblasts model showed a strong correlation between zeta potential and fetal lung transfection. Finally, we assessed the toxicity of LNPs in a tracheal occlusion lung explant model. The optimized formulations appeared to be safe on ex vivo fetal lungs as indicated by insignificant changes in apoptosis (Caspase-3) and proliferation (Ki67) markers. In conclusion, we have optimized an LNP formulation that is safe, with high transplacental transport and preferential transfection in fetal lung cells. Our research findings represent an important step toward establishing the safety and effectiveness of LNPs for gene delivery to the fetal organs.

* Corresponding author at: 209 Victoria Street, ON M5B 1T8, Canada.
E-mail address: hagar.labouta@unityhealth.to (H.I. Labouta).

https://doi.org/10.1016/j.jconrel.2024.10.047
Received 30 July 2024; Received in revised form 23 September 2024; Accepted 21 October 2024
Available online 28 October 2024

1. Introduction

Congenital fetal anomalies occur during pregnancy and are characterized by abnormal fetal organ development, which can result in perinatal mortality or severe lifelong morbidity [1]. These anomalies complicate 3 % to 6 % of pregnancies and are one of the leading causes of infant mortality [2]. Congenital diseases exhibit phenotypic changes due to genetic mutations, chromosomal abnormalities, epigenetic changes, or environmental factors [3]. Many of these congenital diseases are attributed to genetic abnormalities that start at conception, and with advancements in prenatal diagnosis, early intervention to correct the course of the diseases during pregnancy could be possible [1,4,5].

For many congenital diseases, early in-utero intervention by replacing or silencing the gene of interest could restore or improve normal fetal development [1,6]. Viral vectors have been utilized as a vehicle for gene therapies due to their targeting efficiency [7]. However, their development is often limited by challenges such as manufacturing difficulties, high cost [8], and particularly high immunogenicity risks which could be more severe during prenatal development [9]. In contrast, non-viral gene delivery systems based on polymer or lipid excipients are showing promise due to their low immunogenicity, ease of manufacturing, and reproducible physiochemical properties [10,11]. These advantages make non-viral gene delivery systems a potentially safer alternative vehicle for these fetal gene therapies.

Recent advancements in lipid excipients, particularly ionizable lipids, have established lipid nanoparticles (LNPs) as the safe and efficient vehicle for nucleic acid transfection. Compared to previous iterations of lipid-based formulations (e.g., liposomes), these LNPs have shown significant improvement in their efficiency in driving endosomal escape and higher encapsulation efficiency [12]. Endosomal escape is essential for cytosol delivery and protein translation or silencing. Ionizable lipids enable the endosomal escape of LNPs as they get positively charged at endosomal pH which drives the bilayer to hexagonal transition [13,14]. Patisiran, or Onpattro®, was approved in 2018 as the first FDA-approved LNPs formulation for nucleic acid delivery. The formulation included D-lin-MC3-DMA as the ionizable lipid, DSPC as the helper lipid, cholesterol, and DMG-PEG as the PEGylated lipid at molar percentages of 50, 10, 38.5, and 1.5, respectively [15,16]. Since then, different studies and drug development programs have proposed similar formulations or excipients for other targets.

To date there are no clinically approved nanoparticle formulations that can cross the placental barrier to achieve fetal targeting. Earlier, our team developed a novel fetal drug delivery approach by leveraging the natural transfer of passive immunity from the mother to the fetus through the FcRn receptors which transport immunoglobulin G (IgG). Similarly, IgG conjugated chitosan nanoparticles showed higher placental transport compared to bare nanoparticles [17].

Few other studies showed an impact of the physicochemical properties of nanoparticles, including size and surface chemistry, on their transport efficiency across the placenta [18,19]. Most of these studies focused on polymeric and inorganic nanoparticles from the perspective of toxicological studies. However, the limited data available are sometimes conflicting and may require further systematic studies for a more comprehensive validation. This is because many studies that focus on a single characteristic of nanoparticles may not provide accurate predictions for placental transport [19–21]. Therefore, studying multiple properties, such as material composition, surface charge and modifications, and biological factors, could be more capable of modeling placental transport by establishing structure-activity relationships (SAR) [21]. To date, a systematic approach to investigate the transport of LNPs across the placenta is lacking.

In this work, we are adopting a multiparametric approach to develop the first predictive model on the transport of LNPs across the placenta. Given the complexity of the datasets when optimizing new formulations, linear (single cause−effect) models and other algebraic approaches will have difficulty discerning trends from the experimental dataset. On the other hand, machine learning (ML) as a data-driven approach has shown its effectiveness in tackling these challenges and demonstrates potential in the design of drug delivery systems [22,23]. Modeling the relationship between LNPs design parameters and their transplacental transport metrics is critical to inform the development of optimized LNPs for nucleic acid delivery to the fetus for management of congenital anomalies.

Aside from nanoparticle transport across the placenta, it is important to optimize the LNPs formulation to maximize nucleic acid transfection in fetal cells in order to increase the efficacy of the congenital therapy. The impact of LNPs exposure on fetal development should also be assessed. While the cargo delivered, such as siRNA or mRNA, could restore normal development and prevent permanent damage, the delivery vehicle itself could pose toxicity issues on fetal development [24]. To this end, we present here a workflow based on in vitro and ex vivo experiments for initial screening of LNPs formulations for transplacental transport, viability and transfection efficiency using model placental trophoblast and fetal lung cells. Understanding all these parameters is the first step to designing safe and effective congenital therapies during pregnancy.

2. Methods

2.1. Materials

All the lipids were purchased from Avanti Polar, except D-lin MC3 DMA was purchased from MedChemExpress; all the lipids full name are included in Supplementary Table 1. The transwell inserts with pore size 5 μm were purchased from MilliporeSigma Canada (cat: CLS3421-48EA). All the centrifugal filters were purchased from Fisher Scientific (cat: UFC801024, UFC803024, 14558473). AF488-siRNA was purchased from Qiagen (cat: 1027292). FITC-labelled human IgG (cat: F9636), FITC-dextran (cat: FD10S), and TNS reagent (cat: T9792) were purchased from MilliporeSigma Canada. Active Capase-3 antibody (cat: AF835) and iFlour 647-WGA (cat: 25559) were purchased from Cedarlane Labs. Ki-67 antibody was purchased from BD Biosciences (cat: 556003). Primary rabbit ZO-1 antibody (cat: 40–2300) and goat anti rabbit-AF647 (cat: A-21245) were purchased from Invitrogen. Primary rabbit fcRn antibody (cat: ab193148) was purchased from Abcam. Human placental BeWo b30 cells were provided by Dr. Tina Buerki-Thurnherr (EMPA, Switzerland). Human Umbilical Vein Endothelial Cells (HUVEC) was purchased from Lonza (cat: C2519A). Human fetal lung fibroblast (WI-38) was purchased from ATCC. ViaLight Plus Cell Proliferation and Cytotoxicity BioAssay Kit was purchased from Lonza (cat: LT07–221).

2.2. Lipid nanoparticles synthesis

LNPs were formed by hydrodynamic focusing using the 5-inlet microfluidic chip from Dolomite Microfluidics (Norwell, USA). Mixtures of different ionizable lipids, helper lipids, cholesterol, PEGylated lipids were mixed at different molar percentages, as outlined in Table S2, Supplementary Information 2. A rhodamine-B labelled lipid was added to the lipid mixture at a 0.5 M percentage to prepare fluorescent LNPs for tracking using fluorescence measurements and imaging. The final lipid mixture was solubilized in ethanol at a concentration of 2 mg/ml. Using two programmable syringe pumps, the lipid was injected into the middle channel at a flow rate of 15 μl/min while MES buffer, pH 6, 0.1 M, was injected into the side channels at 75 μl/min, achieving a flow rate ratio of 5:1. Following the formation of LNPs, they were centrifuged three times at 2500*g* for 12 min at 4 °C using Amicron centrifugal filters (10,000 Da) to remove ethanol. In each centrifugation round, the LNPs were redispersed in a 3 ml of 10 mM PBS, pH 7.4.

To prepare siRNA-loaded LNPs, AF-488 labelled siRNA was introduced in the aqueous phase (10 mM citrate buffer at pH of 4). The concentration was adjusted to achieve a lipid: siRNA weight ratio of

40:1, 20:1, or 10:1; most formulations have a ratio of 40:1 unless otherwise stated. Rhodamine-B labelled lipid was not used for labelling siRNA-loaded LNPs. For centrifugation of siRNA-loaded LNPs, 30,000 Da filters were used at 1358 g for 10 min at 4 °C, and 3 ml of RNAse-free PBS was added in each centrifugation round. The supernatant was analyzed for fluorescence of unencapsulated siRNA to indirectly determine the encapsulation efficiency.

We used EDC/NHS conjugation reaction to prepare IgG-coated LNPs, in which 3 ml of MES buffer, pH 6, 100 mM was added in each centrifugation round.

2.3. IgG surface conjugation

LNPs were conjugated with FITC-labelled IgG to use FITC fluorescence as a surrogate for IgG density following LNPs conjugation using a plate reader. IgG antibodies are supplied with 15 mM sodium azide for preservation, but this concentration can interfere with conjugation reactions. Therefore, prior to the conjugation reactions, IgG was filtered using 10,000 Da centrifugation filters at 1559 *g* for 10 min and were redispersed in 2 ml sterile PBS.

Different functionalized DSPE-PEG lipids were included in the different formulations at 0.5 M % to achieve IgG conjugation at different orientations. Each functional group requires different reactions for IgG surface conjugation, as detailed in Supplementary Information 1.

2.4. Physicochemical characterization

We measured the size, size polydispersity index (PDI), and zeta potential of all prepared LNPs formulations using a Zetasizer Ultra (Malvern Polyanalytical), which depends on dynamic light scattering.

The number concentration of LNPs, number of particles per ml, was determined using nanoparticle tracking analysis (NTA, ZetaView, Particle Metrix GmbH, Germany). The measurement parameters were optimized to achieve the optimal mean intensity and number of particles per field of view. The pre-acquisition parameters were set as follows: Sensitivity = 70, Shutter = 100, frame rate = 30, and Resolution: Medium. The post-acquisition parameters were as follows: Minimum Brightness = 25, Min Area = 5, Max Area = 1000, and trace length = 15.

Additionally, the apparent pKa of LNPs was measured using the TNS assay, as detailed in Supplementary Information 1.

2.5. IgG surface density and conjugation efficiency

Following FITC-IgG conjugation and centrifugation using 300,000 Da filters, the supernatant with the unbound FITC-IgG was collected and measured for fluorescence using a plate reader using excitation and emission wavelengths of 485 and 528 nm. The concentration of unbound IgG was calculated reference to a 10-point preconstructed calibration curve and the conjugated IgG concentration was calculated indirectly based on the difference from the total theoretical IgG concentration used in the conjugation reaction. From the conjugated concentration, the mass of IgG and the number of IgG in the sample was calculated, and relying on the NTA results, the number of antibodies per LNP (Eq. 1) and the distance between antibodies on the LNP surface (Eq. 2) were calculated.

$$Number\ of\ antibodies\ per\ LNP = \frac{(number\ of\ conjugated\ Antibodies)}{number\ of\ LNPs\ in\ the\ sample} \quad (1)$$

$$Approximate\ distance\ between\ antibodies\ (nm) = \pi \times \sqrt{\left(\frac{(LNP\ Diameter \times 10^{-9})^2}{n\ of\ Antibodies\ per\ LNP}\right)} \times 10^9 \quad (2)$$

2.6. In vitro cell culture models

Each of human placental BeWo b30 trophoblast cells, human umbilical vein endothelial cells (HUVEC) and human fetal lung fibroblast (WI-38) were cultured at 37 °C and 5 % CO_2. Different culture media were used for the different cells. Ham's F12 K Nutrient Mixture, Kaighn's Mod supplemented with L-Glutamine, 10 % FBS and 1 % Penicillin-Streptomycin was used to culture BeWo cells. HUVEC cells were cultured using EBM™-2 Basal Medium supplemented with EGM™-2 SingleQuots™ Supplements (ATCC). WI-38 lung fibroblasts cells were cultured in EMEM supplemented with L-Glutamine and 10 % FBS. Near confluency, cells were sub-cultured using 0.5 % trypsin−EDTA. For this work, we used passages 28–43, 5–9 and 19–22 for BeWo, HUVEC and WI-38, respectively. For transport experiments, cells were cultured on transwell membranes in 24-well plates as summarized in Fig. 2. First, membranes were treated with fibronectin for 2 h to promote the adherence of HUVEC cells on the bottom side (in EBM-2 media) and then BeWo cells were cultured on the side facing the apical compartment (in F12K media). The seeding density and time were optimized to ensure both cells were forming a monolayer without overgrowth. The exposure time of forskolin was optimized to achieve syncytialization, as shown in Supplementary Fig. 1.

For the combined transport and transfection experiment (Fig. 10), lung fibroblasts were additionally seeded on the bottom of the basolateral compartment using EMEM media at a seeding density of 30,000 cells per well prior to seeding the BeWo cells.

2.7. Cell viability study

Cells were seeded in 96 well plates at a density of 10,000 cells per well for 24 h before exposure to different concentrations of LNPs for another 24 h. As a negative control (NC, 100 % viability), some wells were treated with media only (no LNPs) for 24 h. Positive controls (PC, 0 % cell viability) were exposed to triton X-100 for 10 min. We conducted Calcein, ViaLight, and MTT assays, to measure cell viability under different conditions. Please refer to Supplementary Information 1 for the detailed protocol of each assay. For all of these assays percentage cell viability was calculated according to Eq. 3. The viability is normalized to negative and positive controls as established in our previous work [25]. The measured signal represents the output of the assay; it is bioluminescence for Vialight, fluorescence for Calcein, and absorbance for MTT.

$$Viability\% = \frac{Signal_{(experimental)} - Signal_{(\mathrm{PositiveControl})}}{Signal_{(\mathrm{NegativeControl})} - Signal_{(\mathrm{PositiveControl})}} \quad (3)$$

2.8. Lipid nanoparticles transport assays

Prior to transport studies, barrier formation of the different placental models was checked quantitatively using a fluorescence transport assay using 10 kDa FITC-labelled dextran; 100 µl of 42 µg/ml was added to the apical compartment. At different time intervals, 25 µl samples were withdrawn from the basolateral compartment at three time points, diluted suitably with fresh media and assayed using plate reader (excitation and emission wavelengths of 485 and 528 nm). Samples withdrawn were immediately replaced with an equal volume of fresh medium, which was accounted for in the transport percentage calculations. FITC-labelled dextran concentration reference to a 10-point preconstructed calibration curve.

LNPs transport experiments were conducted following the same seeding protocols and using freshly prepared LNPs within 24–48 h of synthesis. A total volume of 100 µl dispersion of rhodamine-labelled LNPs in culture media was added to the apical compartment, representing the maternal side of the placenta. At different time intervals up to 24 h, 25 µl samples were withdrawn from the basolateral compartment (600 µl total), representing the transported LNPs to the fetal

compartment. Samples withdrawn were immediately replaced with an equal volume of fresh medium. Withdrawn samples were diluted suitably and analyzed for fluorescence in black 96 well plates at excitation and emission wavelengths of 560 nm and 600 nm, respectively, and the mass of transported LNPs was determined according to an 8-point standard curve generated for each formulation. Percentage transport was calculated by dividing the fetal side concentration by the equilibrium concentration. The equilibrium concentration was determined by dividing the total mass added to the maternal side by the total volume (the sum of the maternal side volume, 100 µl, and the fetal side volume, 600 µl).

2.9. Transport kinetics models

2.9.1. Kinetic model implementation

A Logistic Growth Model was employed to characterize the transport of LNPs. The logistic growth model is used to describe saturation dynamics typical in biological transport processes, which are crucial for effective nanoparticle permeation through biological barriers, such as the placenta in this work. The logistic model is defined according to Eq. 4.

$$C_t = \frac{C_\infty}{1 + e^{-k(t-t_o)}} \tag{4}$$

Where, C_t is the concentration of nanoparticles at time t, C_∞ is the final equilibrium concentration, and k is the rate constant. Here, t_o represents the inflection point where the growth rate is maximal, effectively indicating the half-maximal concentration time.

2.9.2. Parameter estimation and model fitting

Custom Python scripts were developed to fit the model to the normalized concentration data. The scripts utilized non-linear curve fitting techniques with multiple initial guesses to ensure robust model fitting. Key parameters such as the rate constant (k), half-time ($t_{1/2}$), and the inflection point (t_o) were extracted from the fits.

2.9.3. Apparent permeability calculation

Apparent permeability (P_{app}) was calculated to assess the efficiency of LNPs transport across the placental barrier. The formula used was:

$$P_{app} = \frac{dQ}{dt}\frac{1}{A\,C_o} \tag{5}$$

Where $\frac{dQ}{dt}$ is s the rate of mass transport, A is the effective surface area of the membrane, and C_0 is the initial concentration in the donor compartment. P_{app} is critical for understanding the transport characteristics of nanoparticles, including their interaction with the barrier and transport kinetics.

2.10. Machine learning modeling of transport percentage, transport kinetics, size and zeta potential of lipid nanoparticles

2.10.1. Dataset correlation analysis

The pairwise correlation between all the descriptors (input features and the target) was analyzed. Specifically, Pearson correlation coefficient was computed using pandas.DataFrame.corr. The results were visualized using a heatmap, where red color indicates a positive correlation and blue indicates a negative correlation. The strength of the correlation (i.e., the absolute value of Pearson correlation coefficient values) was indicated by the intensity of the color, with darker colors representing stronger correlations.

2.10.2. Machine learning modeling

To address the imbalance in the Size and Zeta Potential dataset, random over-sampling was applied to ensure a more balanced distribution of feature values. This method involves duplicating instances from the minority class to increase their representation, thus augmenting the dataset and providing the model with more information on the minority class [26].

Input features in all datasets were then standardized using sklearn.preprocessing.StandardScaler. ML models were developed using the scaled dataset to predict the target variables (i.e., transport percentage, transport kinetics, permeability, or half-time). A panel of models, including extreme gradient boosting (XGB), decision tree (DT), random forest (RF), support vector regressor (SVR), light gradient boosting machine (LightGBM), and linear model with least absolute shrinkage and selection operator regularization (Lasso), were developed for comparison. These models were initialized with their default hyperparameters from sklearn, xgboost, and lightgbm libraries.

The models were trained and evaluated using a leave-one-out cross-validation method. The model performance was measured using four metrics to provide a comprehensive evaluation: mean absolute error (MAE), median absolute error (MedAE), root mean squared error (RMSE), and mean squared error (MSE). The model that performed the best across most of these metrics was identified as the best-performing model for further analysis.

2.10.3. Model interpretation and validation

The best-performing model identified from the model evaluations was further analyzed to gain insights into the relationships between the features and the target. Specifically, the model was interpreted using Shapley additive explanations (SHAP) analysis to rank the input features in terms of their importance to the prediction. The results were visualized using shap.summary_plot.

We then validated the ML model using external data not included in the training dataset. We relied on the top 5 features from SHAP analysis to design three new formulations that are expected to have low, moderate, and high transport across the placenta and then tested their transport at 24 h.

2.11. Immunofluorescence imaging of in vitro placental models

We used immunostaining protocols for qualitatively investigating barrier function, confirming FcRn expression and for cell uptake of LNPs following the 24 h transport study, cells were washed with 1× PBS, fixed in 4 % paraformaldehyde and washed three times in sterile PBS, permeabilized using 0.1 % triton x-100 in PBS, and blocked using a mixture of 0.1 % tween-20, 3 % BSA, 3 % serum, 0.75 % glycine in PBS for 1 h at room temperature. Cells were then incubated overnight at 4 °C with the primary antibody, either ZO-1 diluted 1 in 80 or FcRn diluted 1 in 100. After washing, cells were incubated with the secondary antibody, goat anti rabbit-AF647 (diluted 1 in 400) for 40 min at room temperature. Finally, nuclei were DAPI stained and mounted with mounting media and covered with 1.5 mm coverslips. Samples were imaged by a QUORUM SPINNING DISC Confocal system using a 63× Oil objective and an ORCA-Flash 4.0 V2 PLUS sCMOS camera. The imaging parameters are summarized in Supplementary Table 3. We used *Z*-stacks to calculate the sum of pixels due to LNPs associated with the cells in all optical slices following normalization to remove background signal.

2.12. In vitro cell transfection study

Cells were cultured in black 96-well plates till 50–60 % confluency before exposure to LNPs encapsulating 1 picomole or 4 picomole of siRNA, to make a final concentration of 10 nM or 40 nM, respectively. For positive control (PC), cells were exposed to siRNA-Lipofectamine complexes prepared from 0.3 µl lipofectamine and 1 or 4 pmol of siRNA. Cells incubated with media only were used as a negative control (NC). After 24 h of incubation, cells were washed with sterile 1× PBS to remove any unbound LNPs or siRNA, fixed in 4 % PFA (methanol free) for 15 min, then washed with sterile 1xPBS 3 times. We used Alexa Fluor 647-labelled wheat germ agglutinin (WGA-647) for cell membrane

A

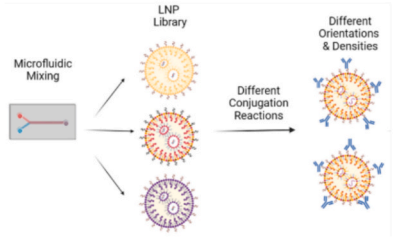

B

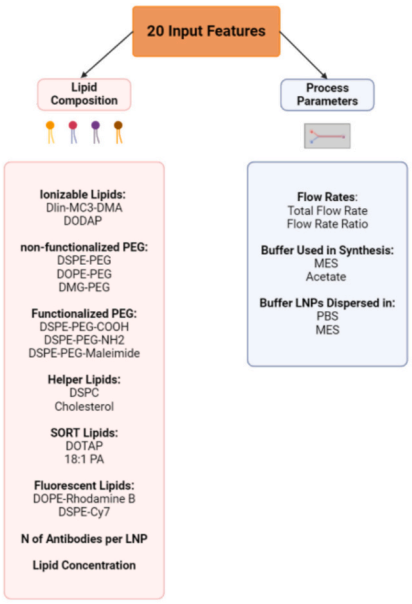

C

Physicochemical properties	Size (nm)	Zeta Potential (mV)
Minimum	68.3	-38.9
1st Quartile	92.5	-15.9
Median	111.8	-4.7
3rd Quartile	135.8	16
Maximum	251.7	46

D

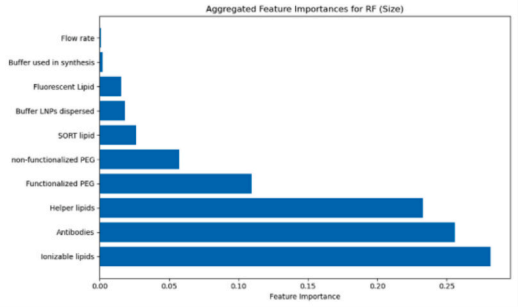

E

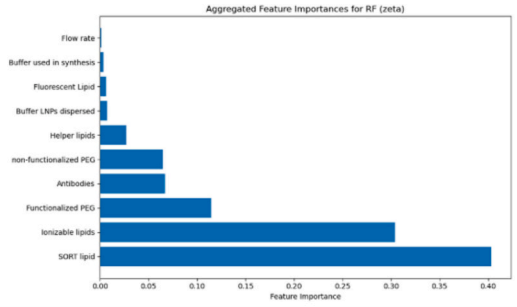

F

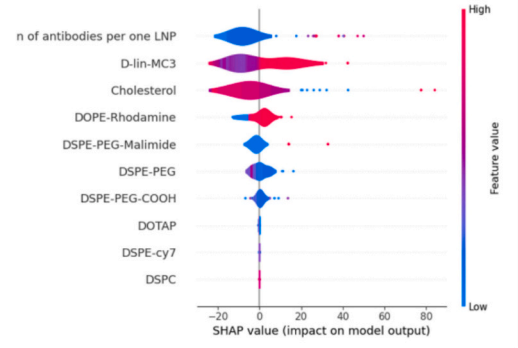

G

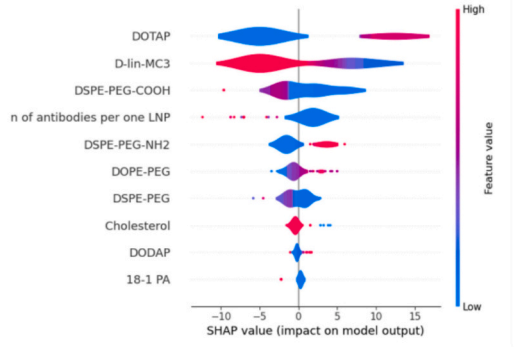

Fig. 1. Synthesis and characterization of lipid nanoparticles (LNPs), and machine learning modeling for size and zeta potential. (A) A schematic of LNPs synthesis using microfluidic mixing followed by IgG surface conjugation; Created with BioRender.com. (B) Overview of the different variables/features used to develop the LNPs library, including lipid classes and process parameters; Created with BioRender.com. (C) Summary of the physicochemical properties of the LNPs library. The aggregated feature importance of each input (variable) including lipid classes and process parameters in predicting the (D) LNPs size and (E) zeta potential by Random Forest (RF) machine learning model. Shapley additive explanations (SHAP) showing the top 10 input features predicting (F) the size and (G) the zeta potential of the LNPs.

staining. The staining protocol varied for the different cell lines. BeWo cells were incubated with 10 μg/ml WGA-647 in HBSS buffer for 10 min, then the nuclei were stained with Hoechst (2 μg/ml in PBS) for 10 min. For lung fibroblasts, a solution of 5 μg/ml WGA-647 was incubated with the cells for 10 min followed by Hoechst at 2 μg/ml for 10 min.

Cell Discoverer machine was used for the transfection experiments as it enables automated high throughput imaging, which enabled the screening of multiple formulations. The imaging parameters are summarized in supplementary table 3. Transfection was calculated based on the mean intensity values from the image analysis. Transfection was presented as a percentage relative to lipofectamine (PC) according to Eq. 6.

$$Transfection\% = \frac{(MI_{exp} - MI_{NC})}{(MI_{PC} - MI_{NC})} \quad (6)$$

2.13. Ex-vivo experiments

2.13.1. Rat fetal lung explant model

We followed a protocol established by our team to harvest the rat embryos on day 18 of pregnancy and dissected fetal lungs [27]. Guided by a surgical microscope, a volume of 10 μl of LNPs formulations was injected into the lung via the trachea using a special microinjection needle described here [28]. Control lungs were injected with 10 μl of PBS each. The trachea was then tied off with a polypropylene surgical suture. The explants were placed on a 12-well plate with a membrane insert. The bottom of the insert was filled with DMEM/F12 media, containing: 8 mM L-glutamine, 100 mg/ mL primocin, 1.0 % FBS. The plates containing explants were left in the incubator for 24 h at 37 °C with 5 % CO2. Then, lungs were formalin fixed for 24 h at 4 °C. Subsequently, lungs were dehydrated in a methanol gradient, cleared in xylene, and embedded in paraffin.

2.13.2. Histological staining

Hematoxylin and Eosin (H&E) staining was performed to study the lung air space. The lung tissue was sectioned using a rotary microtome (Leica, Germany) to produce sections with 5 μm thickness. To ensure reproducibility, an autostainer machine (Leica, Germany) was used to automate the staining process following a pre-set program: Oven 65 °C (10 min), Xylene (3 min,2 min, 2 min), 100 % Alcohol (1 min, 1 min), 95 % Alcohol (1 min), H_2O wash (1.5 min), Hematoxylin (2.5 min), H_2O wash (1 min), DEFINE (acidic solution) (35 s), H_2O wash (1 min), blue buffer (slightly basic solution) (45 s), H_2O wash (1 min), 95 % Alcohol (1 min), eosin (1 min), 100 % Alcohol (1 min, 1 min, 1 min), Xylene (2 min, 2 min). Finally, the slides were mounted and covered with 1.5 mm coverslips.

2.13.3. Immunostaining

We used immunostaining and immunofluorescence imaging to study the effect of LNPs on lung cells proliferation and apoptosis. Lung sections (5 μm) were deparaffinizated using the autostainer using the following program: Oven 65 °C (10 min), Xylene (3 min,2 min, 2 min), 100 % Alcohol (1 min, 1 min), 95 % Alcohol (1 min), H_2O wash (1.5 min). Then the slides were immersed in an antigen retrieval buffer (10 mM sodium citrate, pH 6, with 0.05 % tween-20) and placed in a pressure cooker at 100 °C for 15 min. Following antigen retrieval, the slides were incubated with blocking buffer (PBS with 0.1 % tween-20, 2 % bovine serum albumin, 3 % FBS) for 3 h at room temperature. Sudan black solution (0.1 % in 70 % ethanol) was added for 30 min to reduce autofluorescence. Active Caspase-3 and ki-67 were used as the primary antibodies for Apoptosis and proliferation, respectively. The primary antibody diluted in blocking buffer (Active Caspase-3 to 1 μg/ml or ki-67 to 2 μg/ml) was added to sections and incubated overnight at 4 °C followed by washing 3 times with PBST (PBS with 0.1 % tween-20). Treated lung sections were exposed to the secondary antibody, goat anti rabbit-AF647 or donkey anti mouse-AF647 (10 μg/ml), for 3 h at room temperature followed by washing 3 times with PBST. The nuclei were stained with DAPI (1 in 1000) for 3 min. After washing with PBST, PBS, and double distilled water, the sections were left to dry and were covered with flourmount G and 1.5 coverslips (0.17 mm). The Axioscan slide scanner (ZEISS, Germany) was used to enable high throughput imaging of the lung tissue sections as it enables imaging of the whole section ensuring accurate analysis of the protein expression. The imaging parameters are summarized in Supplementary Table 3. The concentrations of primary and secondary antibodies were optimized to achieve a good signal to background ratio as shown in Supplementary Fig. 9.

2.13.4. Image analysis

Image analysis of the tissue sections was conducted using HALO software (Indica Labs, USA). To measure the airspace of the lung in the H&*E*-stained sections, we used the tissue classifier function that relies on Random Forest algorithms. We first annotated the total area to be analyzed and then calculated the percentage area of air space by dividing the air space area by the total analyzed area.

For immunofluorescence staining experiments, we used two methods for image analysis which are positive pixel counting and the nuclear segmentation method. The region of interest in all analyses was DAPI positive (DAPI+) areas. First, a threshold intensity was determined based on negative control sections, which are treated with secondary antibody only, but were not exposed to the primary antibody. The pixels exceeding the threshold intensity were designated antibody positive (Antibody+). In the nuclear segmentation method, we counted the apoptotic or proliferating DAPI-stained cells that are exceeding the threshold intensity for the antibody. Finally, percentage pixels and cells were calculated using Eqs. 7 and 8, respectively.

$$Percentage of apoptotic or proliferative pixels = \frac{no\ of Colocalized pixels\ (Antibody + \&DAPI +)}{no\ of DAPI + pixels}\% \quad (7)$$

$$Percentage of apoptotic or proliferative cells = \frac{no\ of Apoptotic or proliferative cells\ (Antibody + \&DAPI +)}{Total number of cells\ (DAPI +)}\% \quad (8)$$

2.14. Statistical analysis

Statistical analysis was conducted using GraphPad Prism version 8.0.1 and IBM SPSS software. To compare two groups, the unpaired *t*-test was used for groups with equal sizes. We used the unpaired t-test with Welch's correction to compare groups that were not equal in size. For multiple groups comparison, one-way ANOVA or two-way ANOVA was conducted. First, normality checks and Levene's test were carried out to ensure the assumption of normality was met. If a significant *p* value ($p < 0.05$) was found, the test was followed by post hoc Tukey's test. Significance levels were noted in the figures as follows: * for ($p < 0.05$); ** for ($p < 0.01$); *** for ($p < 0.001$).

3. Results and discussions

3.1. Lipid nanoparticle synthesis using microfluidics

To gain a comprehensive understanding of the interactions of LNPs with the placental barrier, we used microfluidics to create a large library of LNPs (Fig. 1A). This method allows for precise control over the mixing and formation of LNPs, which in turn determines the final size and PDI of the particles [29]. The 5-inlet chip was used for the LNPs formulation, as it enabled the formation of monodisperse LNPs (PDI < 0.25). Our library of LNPs was created by varying the type and percentage of ionizable lipids, non-functionalized PEGylated lipids, functionalized PEGylated lipids (carboxylic acid or amine terminated lipids), and permanently charged lipids (Fig. 1B). The developed LNPs exhibited a broad range of

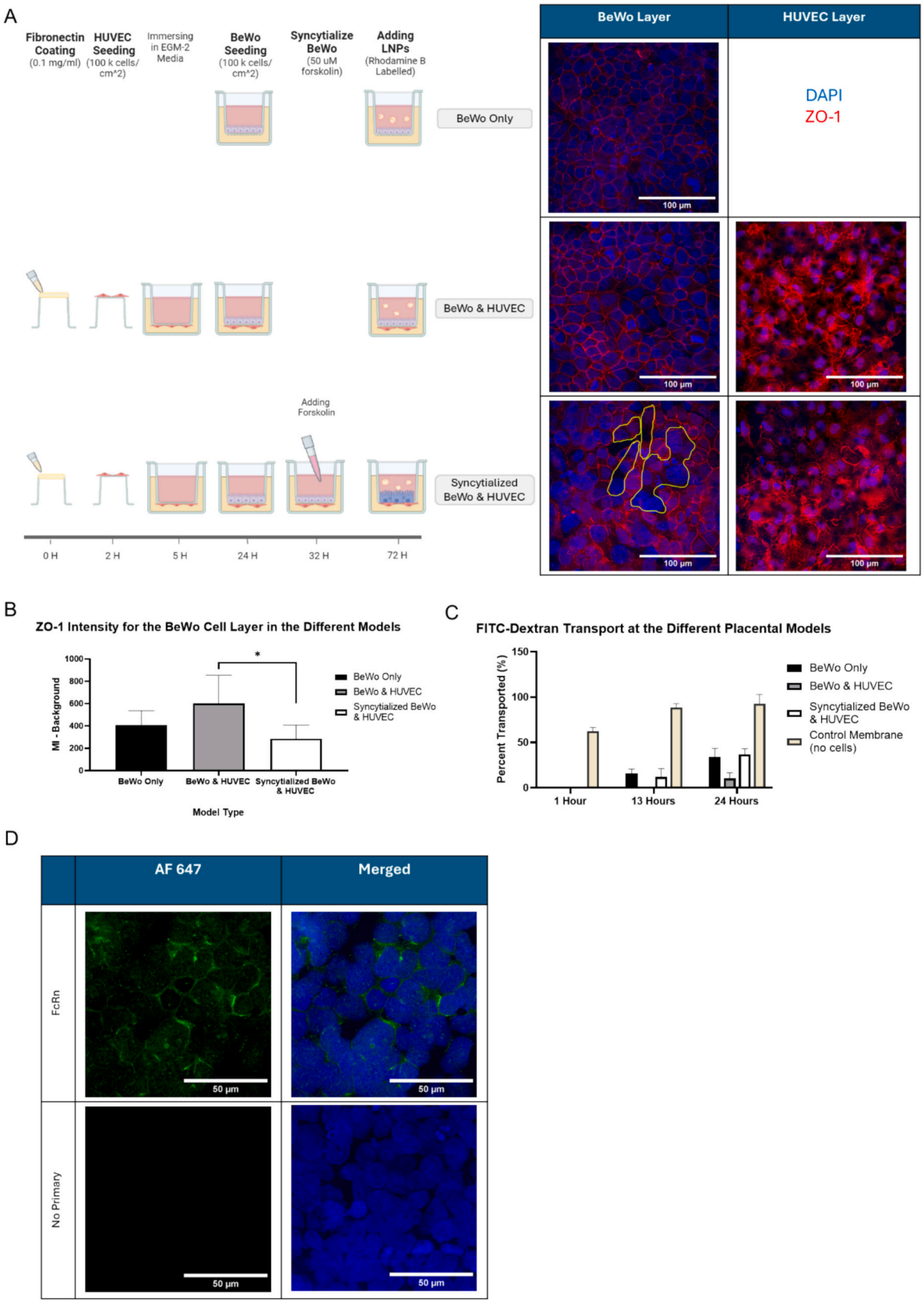

Fig. 2. Development of different placental models. (A) A schematic for cell seeding and other steps for the development of the different models; Created with BioRender.com. For each of these models, we characterized the barrier formation using ZO-1 tight junction staining, denoted in red and syncytialization in which the formation of multinucleated cells is annotated in yellow (B) Comparison of ZO-1 expression levels in the BeWo cells of the different models. (C) FITC-labelled dextran transport across the different placental models at different time intervals. (D) Staining of FcRn receptor (denoted in green) in BeWo cells. Refer to Supplementary Table 3 for imaging parameters. (For interpretation of the references to color in this figure legend, the reader is referred to the web version of this article.)

zeta potentials and sizes. The zeta potential varied from −39 to +46 mV, with a median of −5. The particle sizes ranged from 68 nm to 252 nm, with a median of 112 nm (Fig. 1C). The library of LNPs and their respective physicochemical properties are listed in Supplementary Table 2.

Besides its ease of scalability, high reproducibility, and miniature scale, the microfluidic mixing process is easily programmable to achieve the high-throughput capabilities desirable in ML- driven studies [30]. The LNPs prepared using this microfluidic system were then characterized and complied into a dataset for ML model development, aiming to better understand how the composition and process parameters influence the particle size and zeta potential. The resulting best-performing models were interpreted in terms of feature importance for predicting LNPs size (Fig. 1D) and zeta potential (Fig. 1E). Ionizable lipids, the number of conjugated antibodies, and the helper lipids have the highest effect on the size which confirm previous reports [31,32]. Interestingly, fluid flow rates and the buffers employed had a minimal effect on the size and zeta potential. Collectively, our results show that lipid composition is the key determinant of the physicochemical properties of LNPs.

Among the different lipid types, permanently charged lipids had the highest effect on zeta potential (Fig. 1G). Functionalized PEGylated lipids, such as DSPE-PEG-COOH and DSPE-PEG-NH2, had the second highest effect on zeta potential, despite being used at a small molar percentage of 0.5 %. Previous studies have used functionalized PEG to enable antibody or peptide conjugation to LNPs but did not take their effect on the physicochemical properties into consideration [33,34]. In contrast, our results point out their high impact on zeta potential, which warrants careful consideration in future formulation studies.

We used SHAP analysis to visualize the hierarchy of the significance of the different input feature values on the prediction of the output from the most important (at the top) to the least important (at the bottom) [35], as shown in Fig. 1F and G. In these figures, the blue color represents low feature values, and the red color represents high feature values. In Fig. 1F, where each lipid or feature was studied individually, a relatively high number of antibodies per LNP or high D-lin MC3 molar percentage contributes to a higher LNPs size. Conversely, high cholesterol molar percentages contributes to smaller size, as delineated in a previous study [31]. Additionally, Fig. 1G shows how the lipid molar percentage influences the net zeta potential, with high molar percentages of the permanently cationic lipid DOTAP increasing zeta potential, and higher percentages of D-lin MC3 and DSPE-PEG-COOH decreasing

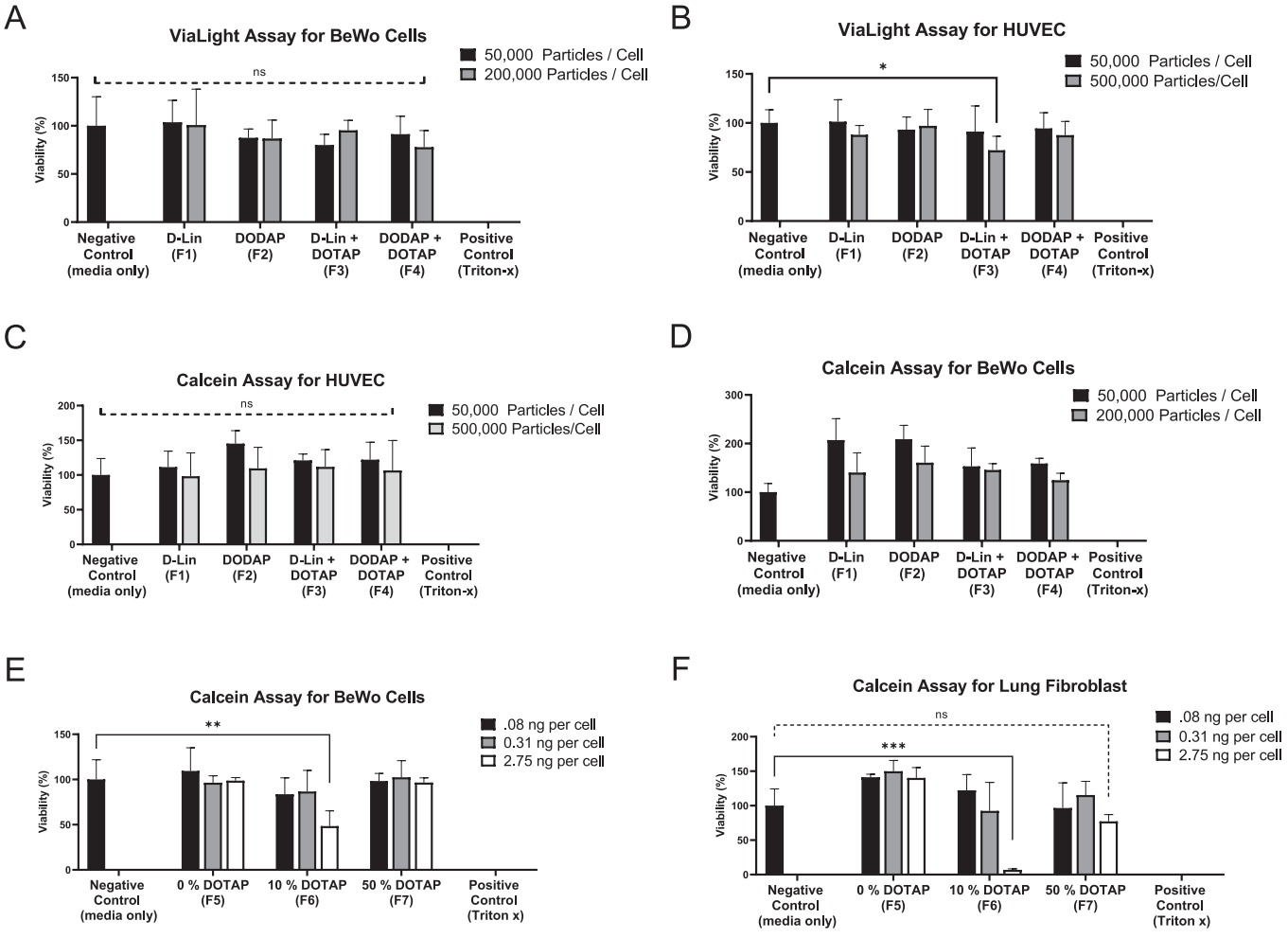

Fig. 3. Cell viability of different cells on exposure to LNPs for 24 h using different viability assays. Data ($n = 6$) are presented as mean ± SD and ns denotes non-significant difference. * ($p < 0.05$); ** ($p < 0.01$); for ($p < 0.001$) denote different levels of statistical significance. Culture media and Triton X-100 were used as negative and positive controls, respectively. (A) Viability of BeWo cells on exposure to different LNPs formulations using ViaLight Assay. (B) Viability of HUVEC cells using ViaLight assay. Viability of (C) HUVEC cells and (D) BeWo cells on exposure to different LNPs formulations using Calcein AM assay. (E) Viability of BeWo cells on exposure to LNPs with different molar percentage of DOTAP using Calcein AM assay. (F) Viability of fetal lung fibroblasts on exposure to LNPs with different molar percentage of DOTAP using Calcein AM assay. The formulation ID number is included between brackets in each figure. Please refer to the Supplementary Table 2 for the detailed description of the LNPs composition and the physicochemical characteristics of each formulation.

it.

Collectively, the developed ML models for the size and zeta potential will benefit future formulations of LNPs by expediting their development stage to attain specific physicochemical parameters. For instance, increasing the ionizable lipid D-lin MC3 molar percentage or conjugating the LNPs with antibodies could increase the size of the LNPs and decrease their zeta potential.

3.2. Placental model development

To evaluate this library of LNPs (a total of 51 transport experiments with 44 formulations), we developed placental transwell models that are ideal for high throughput screening of formulations and are highly reproducible [36]. Aside from the various physicochemical parameters of the different LNPs formulations, there are several variations in the placental barrier when choosing the number and types of cells included. We believe that these variations have partially contributed to the sometimes conflicting results among the published data [37,38]. Some studies have used a model based on a monolayer of trophoblast cells to mimic the maternal side of the placenta [17,38,39], while others have additionally included endothelial cells as a surrogate of the fetal vessels [37,40,41]. Moreover, some have chemically induced trophoblast syncytialization, aka trophoblast cells fusion, using forskolin to form multinucleated syncytiotrophoblasts [41]. Therefore, we developed three different models to investigate the impact of endothelial cells and syncytialization on LNPs transport, as depicted in Fig. 2A.

First, cell seeding density and time were optimized to establish a confluent monolayer of BeWo cells, as increasing the seeding density or incubation time could lead to overgrowth and multilayer formation, thus hindering the functionality of the barrier [42]. As shown in Fig. 2A, ZO-1 tight junction staining confirmed the formation of the barrier. After treatment with forskolin, we observed a reduction in the number of nuclei per image field (Supplementary Fig. 1) and an increase in their size. The formation of syncytia was also observed, as highlighted in yellow in Fig. 2A. In addition, the intensity of tight junction staining decreased, as shown in Fig. 2B. All these observations are hallmarks of syncytiotrophoblast formation as reported in previous studies [41,43].

We then used a FITC-dextran transport assay to quantitatively evaluate the barrier function of the different models [17,40]. The transport of 10 kDa FITC-tagged dextran was significantly lower in the BeWo model versus in the control experiment without cells and the transport increased gradually over 24 h to around 34 % dextran transport (Fig. 2C). Inclusion of a layer of endothelial cells decreased transport, which was also observed in previous studies [41]. However, this is contrary to results by Aengenheister et al. who observed no effect on 40 kDa dextran transport [40]. On the other hand, we observed a significant increase in dextran transport on exposure of the BeWo & HUVEC model to forskolin. This aligns with an earlier report showing an increase in dextran transport after syncytialization which was justified by the smaller thickness and higher permeability of the syncytiotrophoblast [38]. However, the impact of forskolin-induced trophoblast syncytialization is a contradictory topic. For instance, Wong et al. showed no effect of syncytialization on 4 kDa and 70 kDa dextran transport [41], and Zhou et al. observed a decrease in dextran transport following syncytialization [37]. These two studies used the same forskolin concentration of 50 μM as we did and the differences observed might be attributed to differences in seeding time, forskolin exposure duration, and dextran concentration.

Finally, we characterized the models for FcRn receptor expression which plays a principal role in the transport of IgG antibodies from the mother to the fetus [44,45], which we are employing as a parameter to induce IgG transport in this study. Our immunostaining experiments confirmed the expression of the FcRn receptor in the trophoblast cells used, as shown in Fig. 2D. Altogether, we validated the models for barrier function and FcRn receptor expression allowing us to conduct transport studies of LNPs using these models.

3.3. Cell viability on exposure to LNPs

Prior to conducting a thorough transport study, it was important to screen HUVEC and BeWo cells for cell viability after exposure to LNPs. First, interference between LNPs and the different assay reagents was checked, and no interference was detected. We then measured HUVEC and BeWo cell viability following 24 h exposure to different concentrations of four LNPs formulations representing the diverse chemical compositions and with significantly different zeta potentials and pKa. We used two assays, namely ViaLight and Calcein assays. ViaLight bioluminescent assay detects cellular ATP levels, while Calcein AM fluorescent assay depends on endogenous esterase activity and plasma membrane integrity. Negative (normal media) and positive controls (triton-x 100 treated) were included in all the experiments, representing 100 % and 0 % viability, respectively.

Cell viability was relatively high for all tested formulations ranging from 72 % to 100 % or more. The increased mean viability of cells after 24 h LNPs exposure could be due to cell proliferation over time in the presence of phospholipids and cholesterol, that are naturally present in cell membranes of mammalian cells, as shown in Fig. 3C, D, and F [46,47]. No significant difference in cell viability was observed for all tested LNPs, except in HUVEC cells exposed to LNPs formulation F3 (D-lin + 50 % DOTAP) at a concentration of 500,000 particles per cell. In this case, the mean cell viability was 72 % when analyzed using ViaLight assay, but there was no significant difference compared to the negative control when analyzed using Calcein AM assay as shown in Fig. 3B and C, respectively. Transport experiments included only LNPs concentrations in the safe (non-toxic) range.

Cell viability assays were also needed to determine the concentration range for LNPs formulations used for siRNA transfection assays included in our study. Formulations with different molar ratios of cationic lipid DOTAP were tested at different concentrations on BeWo Cells and lung fibroblasts, as shown in Fig. 3E and F. The concentrations tested were 0.08, 0.31, and 2.75 ng per cell. The F6 formulation (with 10 % DOTAP) showed significant toxicity to BeWo cells and lung fibroblasts as shown in Fig. 3E and F, but only at the extremely high concentrations of 2.75 ng per cell. This result can be explained by the hormesis effect; which implies a biphasic dose-response where low dose can lead to beneficial effect while the high dose can be toxic [48]. Nanoformulations containing permanently cationic lipids were previously shown to induce cell toxicity at high concentrations, as they destabilize the cell membrane and inhibit the Na+/K+ pumps [49,50]. Therefore, 0.08 and 0.31 ng per cell concentration were selected for the next transfection experiments following the transport study; considering a lipid to siRNA mass ratio of 40, these concentrations would translate to siRNA concentrations of 10 nM and 40 nM per well (0.35 mm^2).

3.4. Impact of lipid nanoparticles formulation composition and placental barrier design on lipid nanoparticles transport

We then conducted an extensive transport study for the different formulations using the BeWo only model unless otherwise indicated; the BeWo & HUVEC and the syncytialization models were investigated with several formulations. In all of the conducted experiments, the percentages transport were normalized relative to a corresponding control LNPs formulation tested at the same time. This control formulation has D-lin MC3 as the ionizable lipid, DSPC as the helper lipid, cholesterol, DSPE-PEG_{2000} as the PEGylated lipid, DSPE-PEG-COOH as the functionalized PEGylated lipid, and DOPE-Liss Rhod at molar percentages of 49.75, 9.95, 38.3, 1, 0.5, and 0.5 respectively.

IgG functionalization was the first parameter to test as our team has earlier reported that IgG conjugated chitosan nanoparticles can leverage the neonatal FcRn receptor to increase transport across the placental barrier [17]. The crystallizable fragment Fc fragment of IgG induces the transplacental transport via binding with the FcRn receptor in the placental barrier [51]. On the contrary, another study by Gruber et al.

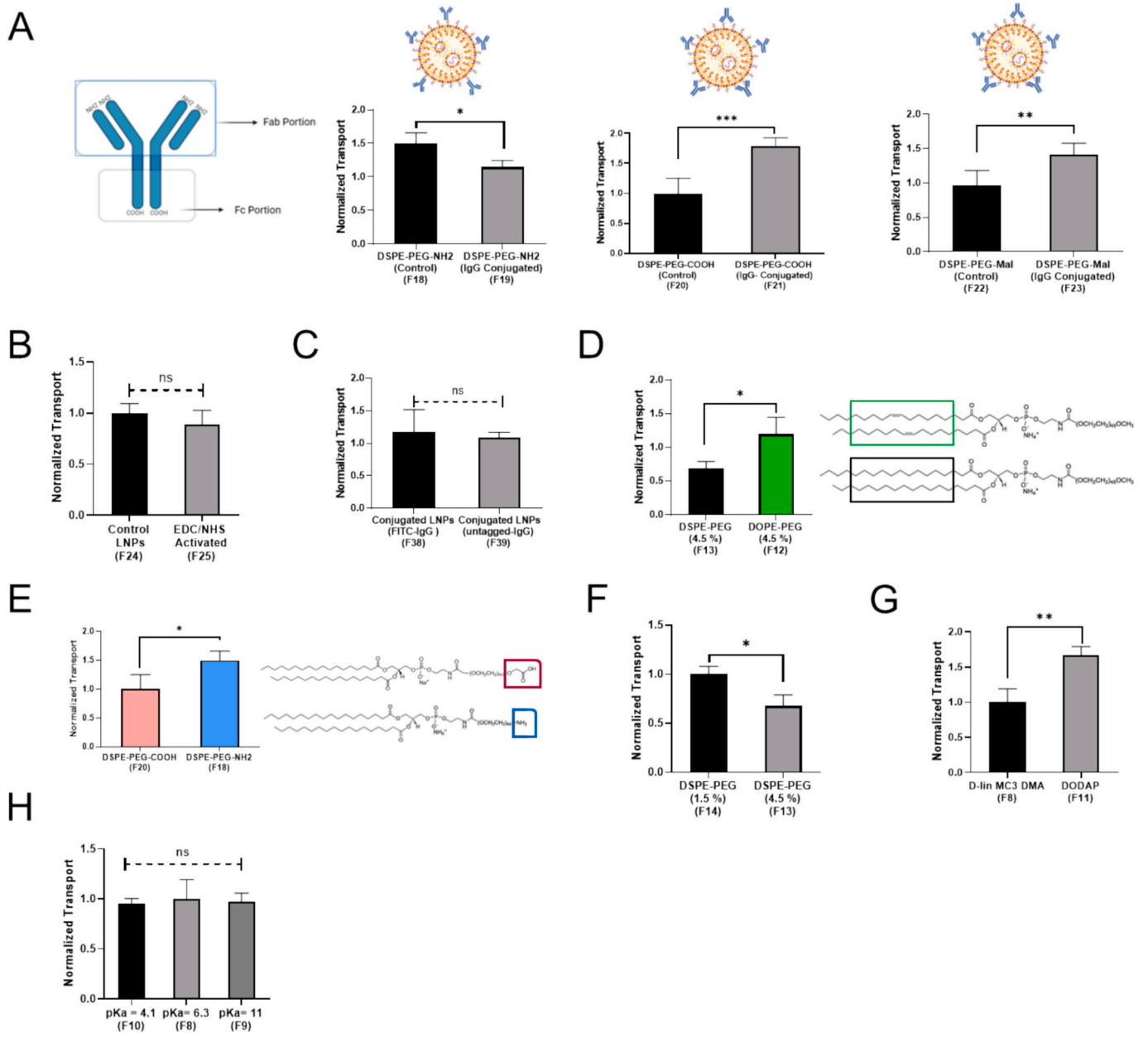

Fig. 4. The effect of LNPs formulation composition on LNPs placental transport. (A) The structure of Immunoglobin G (IgG) antibody and the effect of IgG orientation on the placental transport of different IgG-conjugated LNPs versus unconjugated LNPs; Created with BioRender.com. (B) The effect of EDC/NHS activation on LNPs transport. (C) The effect of IgG labelling on placental transport. (D) The effect of PEGylated lipid tail unsaturation on transport. (E) The effect of PEGylated lipid end-functional group on transport. (F) The effect of molar percentage of the PEGylated lipid. (G) The effect of ionizable lipid on transport. (H) The effect of LNPs apparent pKa on transport. To normalize transport results along our study, we divided the percentage transport of every studied formulation by the percentage transport of a control LNPs formulation that was used across all the experiments. The formulation ID for LNPs is included between brackets in each figure. Please refer to the Supplementary Table 2 for the detailed description of the LNPs composition and the physicochemical characteristics of each formulation.

showed that incubating polystyrene nanoparticles with IgG did not improve placental transport [52]. The different results in transport of IgG treated nanoparticles in these previous studies could be related to the different orientation of the surface IgG, in addition to the different physicochemical parameters of the nanoparticles in both studies. Therefore, it was necessary to test IgG functionalization as a mechanism for fetal delivery using LNPs as the gold standard for nucleic acid delivery, and to optimize the IgG-conjugated LNPs formulation to induce the highest LNPs transport across the placenta.

We first tested how the orientation of IgG attached to the surface of LNPs plays a role in dictating the transport of LNPs across the placental barrier. We hypothesized that high binding to the FcRn receptor is facilitated when many surface IgG have their Fc portion remain free, non-substituted and directed toward the outer part of the conjugated protein to be available for interaction with the receptor. To this end, we prepared different LNPs incorporating 0.5 M percentage of functionalized PEG-lipids with various terminal functional groups, namely carboxylic acid, amine, and maleimide, and used different reactions to conjugate IgG to the LNPs with different dominant IgG orientations. As shown in Fig. 4A, the formulations with DSPE-PEG-COOH and DSPE-PEG-Maleimide showed a significant increase in transport when conjugated with IgG. Since these formulations react with the available primary amines at the end of the Fab portion or the 20 lysine residues available across the IgG chain [53–56], this can reduce the steric

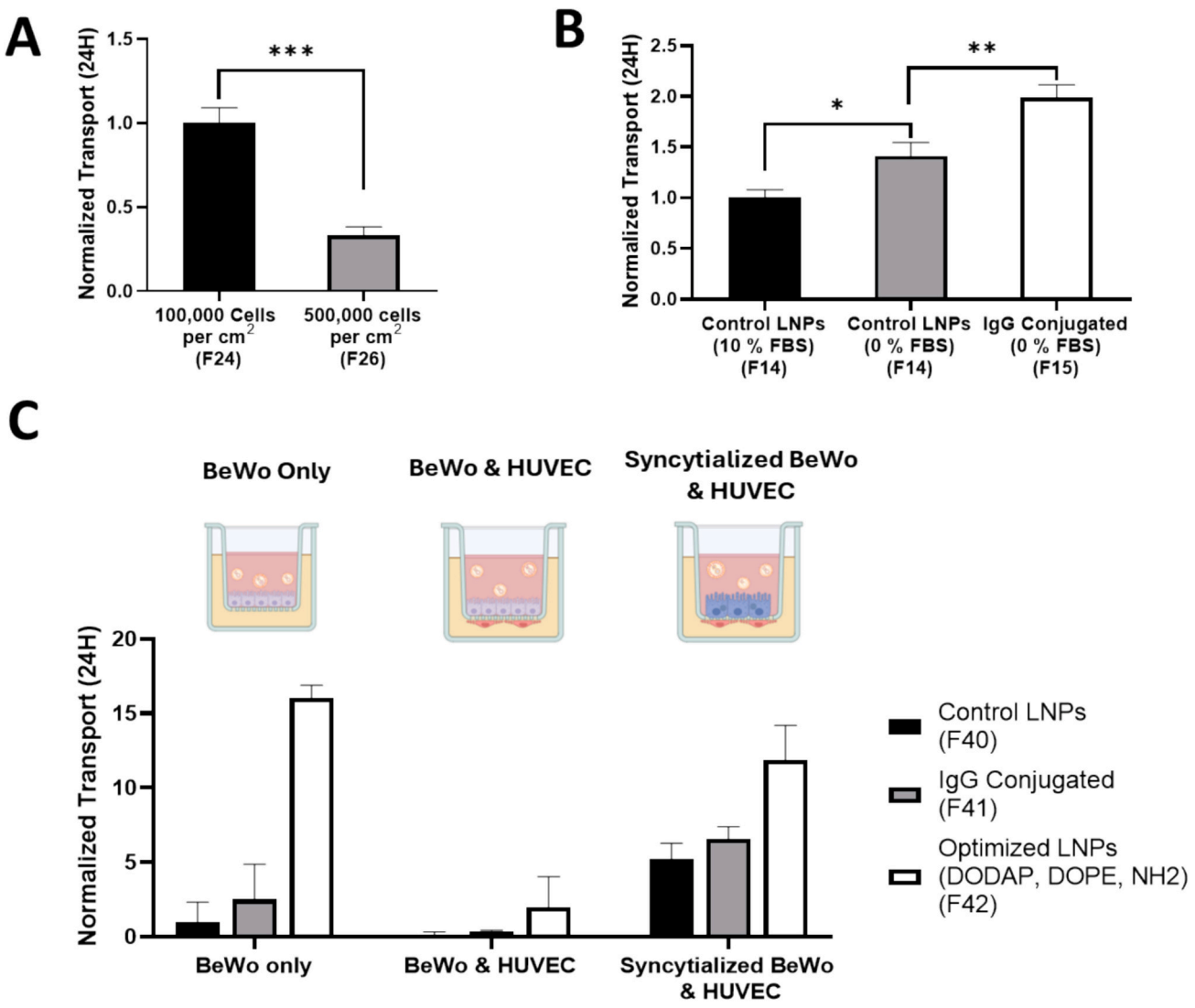

Fig. 5. The placental barrier design features affect LNPs transport at 24 h. (A) The effect of BeWo cells seeding density on LNPs transport. (B) The effect of the percentage of fetal bovine serum (FBS) in the culture media on placental transport. (C) The transport of different LNP formulations across the different placental models. To normalize transport results in our study, we divided the percentage transport of every studied formulation by the percentage transport of a control LNPs formulation that was used across all the experiments. The formulation ID for LNPs is included between brackets in each figure. Please refer to Supplementary Table 2 for a detailed description of the composition and characterization of each formulation.

hindrance near the Fc portion, resulting in more availability for the interaction with the FcRn receptor. However, the formulations with DSPE-PEG-NH2 react with the carboxylic acid groups in the Fc portion [57], leading to steric hindrance that could reduce the interaction with the FcRn receptor. Surprisingly, these formulations showed a significant decrease in transport by 25 % when conjugated with IgG relative to control unconjugated LNPs. This could be attributed to the different physicochemical properties of these LNPs versus controls.

For formulations containing DSPE-PEG-COOH, the carboxylic acid groups were activated by EDC and sulfo-NHS to form an intermediate NHS ester before IgG conjugation. Although this NHS ester is stable for a short time at physiological pH [58], we wanted to test if potentially free esters not functionalized with IgG have any contribution to the transport results. So, we compared the transport of EDC/NHS-activated LNPs to that of control LNPs. We observed no effect on transport, as shown in Fig. 4B. Further, previous studies have pointed out that antibody labeling can affect the antigen-binding specificity [59]; the fluorescent IgG has around three FITC molecules per one IgG according to the manufacturer's information. We, however, observed no significant difference in percentage transport of LNPs conjugated with FITC-labelled IgG when compared with LNPs conjugated with unlabeled IgG, as shown in Fig. 4C.

We then investigated the impact of type and percentage of PEGylated lipids as they are key components of LNPs and are included in all FDA-approved LNPs [60], but their type and percentage are usually varied between formulations. Also, the impact of PEGylated lipids on the physicochemical parameters of nanoparticles, their transfection efficiency, cellular uptake of nanoparticles, and their pharmacokinetics have been established [61]. However, the impact of the type and percentage of PEGylated lipid remains to be investigated in regard to LNPs transport across the placenta.

The PEGylated lipid consists of three main components: the lipid tail, PEG chain, and the PEG-end-functional group. The PEGylated lipid characteristics are influenced by the length and saturation of the hydrophobic tail. Both have a critical effect on the packing of the lipids and the phase transition temperature. As the phase transition temperature decreases, the PEGylated lipid dissociation from the formulation, or dePEGylation, increases [61,62]. We therefore compared the trans-placental transport of LNPs with two different PEGylated lipids, DSPE-PEG and DOPE-PEG. Both have the same head group and tail length

but differ in the degree of tail unsaturation (Fig. 4D). Interestingly, introducing unsaturation, two double bonds, in the lipid tail for DOPE-PEG led to a significant increase in the transport of the LNPs by 75 %. This could be explained by the faster dissociation of DOPE-PEG from the LNPs leading to higher chances for permeation and transport.

Despite being used in a small percentage in our LNPs formulations, the PEGylated lipid-end functional group had a major impact on LNPs' transport. Replacing 0.5 % DSPE-PEG-COOH with 0.5 % DSPE-PEG-NH2 in our LNPs formulation has led to a significant increase in LNPs transport by 51 %, as shown in Fig. 4E. This is most likely due to the increase in zeta potential from −13.1 to +6.6 mV, respectively.

We also investigated the impact of PEGylated lipid percentage on LNPs transplacental transport. In Fig. 4F, two formulations with the same components but different PEGylated lipid percentages were tested. These formulations, F13 (4.5 % PEGylated lipid) and F14 (1.5 % PEGylated lipid) showed no significant difference in zeta potential (−16.7 mV and − 21.2 mV, respectively; Supplementary Information 2). However, the increase in the PEGylated lipid percentage from 1.5 % to 4.5 % led to a significant reduction in transplacental transport. This could be due to lower cellular uptake, as observed in our cell association study in Section 3.6, or decreased permeation through the tight junctions. An increase in PEGylated lipid percentage has also been shown by others to decrease mRNA transfection [63].

Ionizable lipids are the major component of an LNPs formulation, usually constituting a molar percentage ranging from 40 to 50 % per LNP. Ionizable lipids play an essential role in the endosomal escape of LNPs [14] and changing the type of the ionizable lipids can alters the physicochemical properties of LNPs, such as zeta potential and pKa, impacting LNPs transfection efficiency, toxicity and biodistribution [64]. As shown in Fig. 4G, replacing the D-lin MC3 ionizable lipid with DODAP has led to a significant increase in transport by 67 %. This could be attributed to the difference in zeta potential and/or pKa, since incorporation of DODAP instead of D-lin MC3 in LNPs formulation has increased the zeta potential and pKa from −14.4 to +7.8 mV and 6.26 to 6.84, respectively.

Incorporating permanently charged lipids in LNPs, or selective organ targeting technology (SORT), led to promising results for extrahepatic delivery. Specifically, adding 50 % DOTAP or 30 % 18:1 PA to the standard formulation of Onpattro resulted in preferential accumulation in the lung or spleen, respectively [65]. This change in biodistribution was attributed to the difference in the pKa of the LNPs [66]. In our study, we tested the impact of pka as a result of incorporation of a different percentage of permanently charged lipids, namely DOTAP and 18:1 PA, in the LNP formulations on their transplacental transport in vitro. However, LNPs with various pKa values, 4.1, 6.3 and 11, showed no significant differences in transplacental transport ($p > 0.05$), as shown in Fig. 4H. Studying the effect of pKa on LNPs in vivo placental transport warrants further investigation.

Aside from the composition of LNPs formulations, we investigated the impact of different parameters related to the cell model used, namely cell seeding density, IgG concentration in the culture medium and trophoblast syncytialization.

Optimizing the seeding density is an essential step for barrier formation to ensure the formation of a confluent monolayer [42]. For example, a seeding density of 1 million cells per cm^2 showed multilayer formation, while 30 thousand cells per cm^2 had few gaps after 3 days. The 100,000 cells/cm^2 is a typical seeding density in placental barrier formation studies [41]. When one LNPs formulation was assessed at the different seeding densities, it showed a significantly lower transport percentage at the high seeding density, as shown in Fig. 5A. This decreased transport most likely results from the trapping of the nanoparticles at the tight junctions, which is an expected behavior for tightly packed cells [67].

We previously demonstrated the importance of the media IgG concentration when targeting FcRn receptor to induce transplacental transport, as the free IgG can compete with the IgG-conjugated nanoparticles [17]. Since the fetal bovine serum (FBS) contains a high percentage of IgG, we studied LNPs transport in the control media (F12K containing 10 % FBS) and a growth media containing only bovine serum albumin (F12K with 0 % FBS). Surprisingly, control LNPs showed higher placental transport in the case of (0 % FBS), compared to (10 % FBS), as shown in Fig. 5B; it could be due to the significant reduction in tight junction formation, as indicated by ZO-1 expression in Supplementary Fig. 1. Besides, this difference in transport could be attributed to the different protein corona that can form on LNPs in the two medias, as suggested by Gruber et al [52] IgG conjugation further increased LNPs transport ($p < 0.01$) compared to control LNPs.

The fusion of placental trophoblast cells leads to the formation of the syncytiotrophoblast consisting of an interconnected cytoplasm containing multiple nuclei. Syncytialization is critical for a successful pregnancy, as it enables the interchange of substances between the mother and fetus, without transplacental passage through the intercellular junctions, in addition to other placental functions [68]. The effect of syncytialization on the transplacental transport of nanoparticles is still understudied. This represents a knowledge gap in how the nanoparticles interact with the placenta at the different stages of pregnancy. We therefore tested different LNPs formulations in three placental models, as shown in Fig. 5C. We observed a significant increase in the transport for all the LNPs formulations on syncytialization of the BeWo & HUVEC model. Besides, the difference in transport between the different LNPs formulations was reduced on induction of syncytialization. For instance, the optimized LNPs formulation F42 showed 126 % higher transport when compared to the control formulation (F40) in the syncytialized model. This contrasts with 1200 % and 1500 % increase in transport when using the BeWo & HUVEC and BeWo only models, respectively. This indicates an overall increase in permeability regardless of the composition of the LNPs.

Combining the results of the FITC-dextran transport in Fig. 2C and transport of the LNPs in Fig. 5C indicates that the effect of syncytialization could be size-independent. Dextran has an average molecular weight of 10,000 Da, while the LNPs are millions of daltons. However, there're key distinctions between dextran and LNPs in terms of composition and properties, so this point warrants further investigation. In a previous study by Kouthouridis et al., the effect of syncytialization on transport was shown to be size-dependent. They have shown statistically significant increase in 4 kDa dextran transport following syncytialization, while the increase in 65 kDa dextran transport was not statistically significant [38]. Besides, they attributed the transport increase to the smaller thickness and increased permeability of the syncytiotrophoblast layer compared to trophoblast cells [38]. However, we didn't observe a decrease in the thickness of the BeWo layer after syncytialization, as shown in Supplementary Fig. 1. Additionally, we are suggesting that what drives higher placental transport, in the case of syncytialization, is the increase in cellular permeability or cellular uptake as we observed higher LNPs uptake into the Bewo and HUVEC cells, as shown in our LNPs association study in Fig. 8I and H, respectively.

In summary, our comprehensive transport studies highlight the multifaceted factors influencing transport of LNPs across the placental barrier, including the impact of IgG functionalization, PEGylated lipid characteristics, ionizable lipids, and cell model variations. Our findings indicate that both the composition of LNPs and the conditions of the placental model significantly affect transport efficiency. However, our studies could not answer what features of the LNPs and cell model were most important for transplacental transport. For example, is LNPs composition more predictive than IgG functionalization or any of the other studied features? To this end, we used ML to investigate the impact of these LNPs and model related features on their transplacental transport.

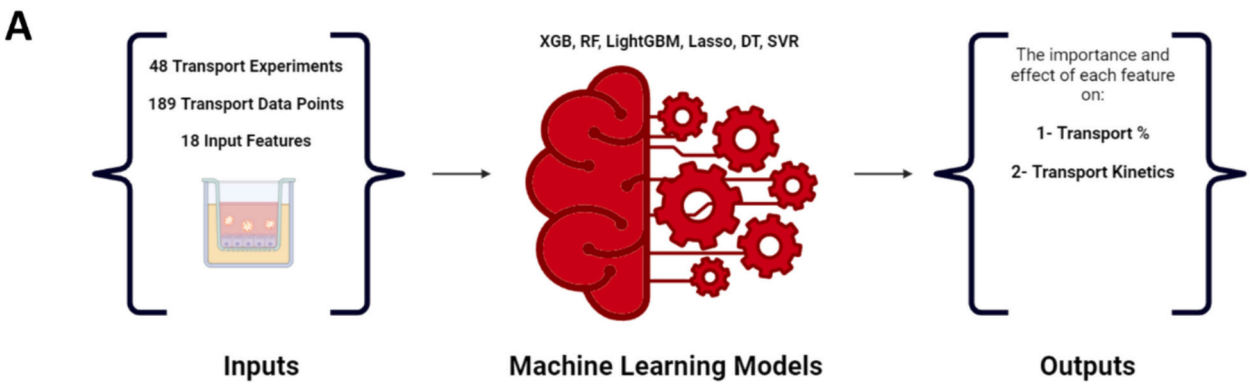

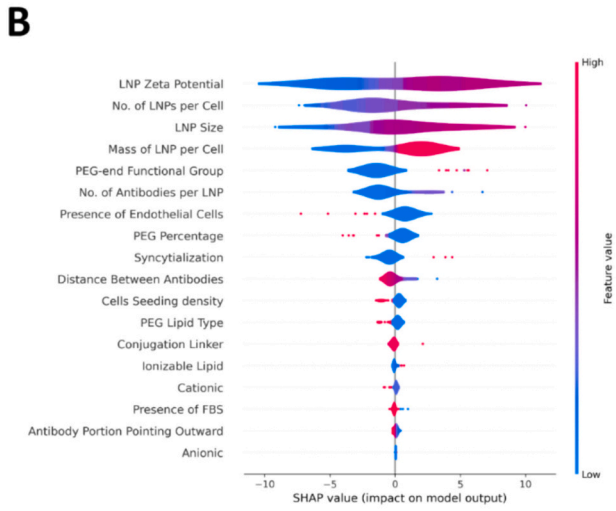

24 H Transport (%)	Mean	Min	Max
	26	0.49	87.5

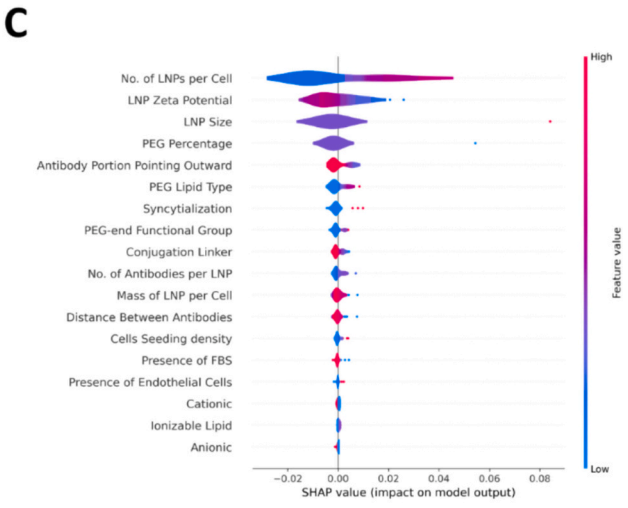

K-value	Mean	Min	Max
	0.104	0.046	0.328

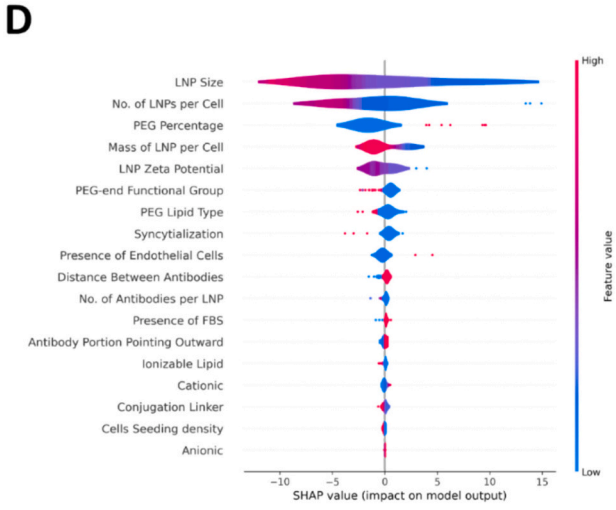

T- half (hours)	Mean	Min	Max
	37.4	6.6	75.6

E

Categorical Variables			
Feature Value	Low	Med	High
PEG-end Functional Group	COOH	Maleimide	NH2
PEG Lipid Type	DSPE-PEG		DOPE-PEG
Ionizable Lipid	D-lin MC3		DODAP
Syncytialization	No		Yes
Presence of Endothelial Cells	No		Yes
Presence of FBS	No		Yes
Antibody Portion Pointing Outward	Fc		Fab
Conjugation Linker	CarboxylNHS		Thiol- Malemide

Fig. 6. Machine Learning Modeling for Percentage Transplacental Transport at 24 h and Transport Kinetics. (A) Schematic describing the dataset and the employed machine learning algorithms used for modeling; Created with BioRender.com. (B) SHAP figure ranking the predictors of the percentage transport at 24 h, using Random Forest (RF) model. (C) SHAP figure ranking the predictors of the transport constant, k-value, of the logistic growth kinetics model, using RF model. (D) SHAP figure ranking the predictors for the t-half of the logistic growth kinetics model, using the RF model.

A

ID	Zeta potential	N of LNPs per cell	Size	Mass of LNP per cell (ng)	PEG-end Functional Group	24 H Transport %
F49	-7.1	152941	98.1	0.15	COOH	8.5
F50	8.56	550000	101.7	0.65	COOH	19.5
F51	26.7	530790	114.8	0.65	NH2	61.4

Low Feature Value Moderate Feature Value High Feature Value

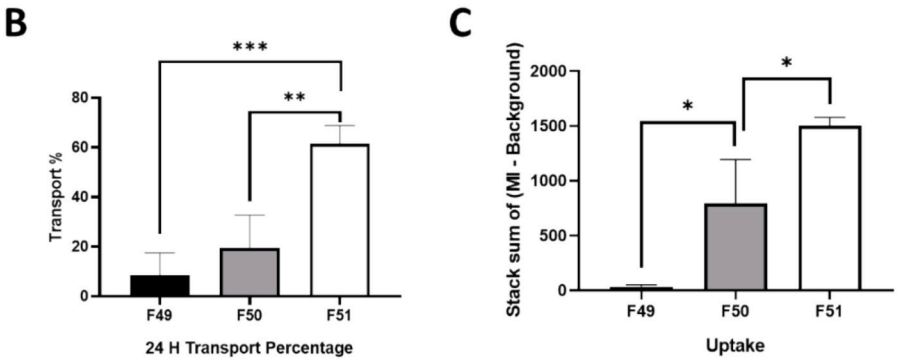

Fig. 7. Machine Learning Modeling Validation. (A) Description and results of the three formulations that were designed to validate the top five influential features on percentage transport at 24 h. (B) The 24 h transport percentage for the three formulations. (BC) The association of LNPs with Bewo cells for the three formulations. The formulations IDs are included in each figure. Please refer to the Supplementary Table 2 for the detailed description of the LNPs formulation compositions and the physicochemical characteristics of each formulation.

3.5. Machine learning modeling for placental transport and transport kinetics of lipid nanoparticles

As mentioned earlier, ML models show promise in analyzing the dataset to provide valuable insights, which can guide the design of future experiments. In this study, the ML approach was employed as a means of analyzing the key attributes to LNPs transport. ML models were trained on an experimental dataset with 189 data points, each representing 3 to 5 replicates, including 18 characteristic input features describing the transplacental transport. The overarching goal of these ML experiments was to address the multidimensional nature of LNPs transport that cannot be retrieved by single factor experiments.

First, we refined the dataset to remove any transport experiments with missing inputs or remove highly dependent features. The refined dataset included 48 distinct transport experiments with 18 input features (Supplementary Information 3). A selection of ML models was trained on this refined dataset using the leave-one-out cross-validation technique, which ensures comprehensive data utilization, a valuable approach for such relatively small datasets. The models' accuracy was evaluated according to four metrics: MAE, MedAE, RMSE, and MSE, as shown in Supplementary Fig. 6. The model, achieving the lowest error in most of these metrics, was chosen for further analysis. The Random Forest (RF) model showed the highest accuracy (lowest error) for predicting the studied outputs: 24H transport percentage, t-half and k-value, as detailed in the Supplementary Fig. 6.

SHAP analysis was used to rank the feature importance from top (highest) to bottom (lowest). The color represents the input feature value; if the feature values are continuous, the blue color represents low values, while red represents high values. However, if the input feature has categorical values, as in the case with the ionizable lipid type or the PEG-end functional group, the color is assigned as detailed in Fig. 6E. The accuracy and reliability of the ranking diminish as you move down in the figure. Therefore, our discussion is focused on the top features in each graph to avoid over-interpretation.

We initially used percentage transport at 24 h as the output for one of the ML models since it was consistent timepoint across all the transport experiments. The mean value for the 24-h time points in the dataset was 26 %. Interestingly, the zeta potential of LNPs was found to be the most critical feature in predicting the total transport percentage, as shown in Fig. 6B. This means that, in the context of this study, high zeta potential is one of the key attributes for high placental transport, while low zeta potential is a predictor for low transport. These observations align with the literature, which reports positively charged nanoparticles tend to interact with the negatively charged cellular membrane, tight junctions, or serum proteins, which could play a role in the transport process [69]. Previous studies that assessed two or three formulations with distinct zeta potential have found no effect from surface charge on transplacental transport of other types of nanoparticles [19,70]. However, our ML model that is based on a dataset which includes various formulations covering a wide range of zeta potentials has provided validated conclusions. Therefore, our study suggests that future nanoparticle transport studies should consider zeta potential as an important feature of LNPs. Based on our ML models illustrated in Fig. 1E, the lipids that most significantly influence zeta potential are, in order: permanently charged lipids, functionalized PEGylated lipids, and ionizable lipids.

Another important feature for percentage transport at 24 h was LNPs size, with bigger sizes leading to increased transport and smaller sizes leading to decreased transport. This contradicts previous studies that showed the opposite correlation [18]. We think our conclusion here

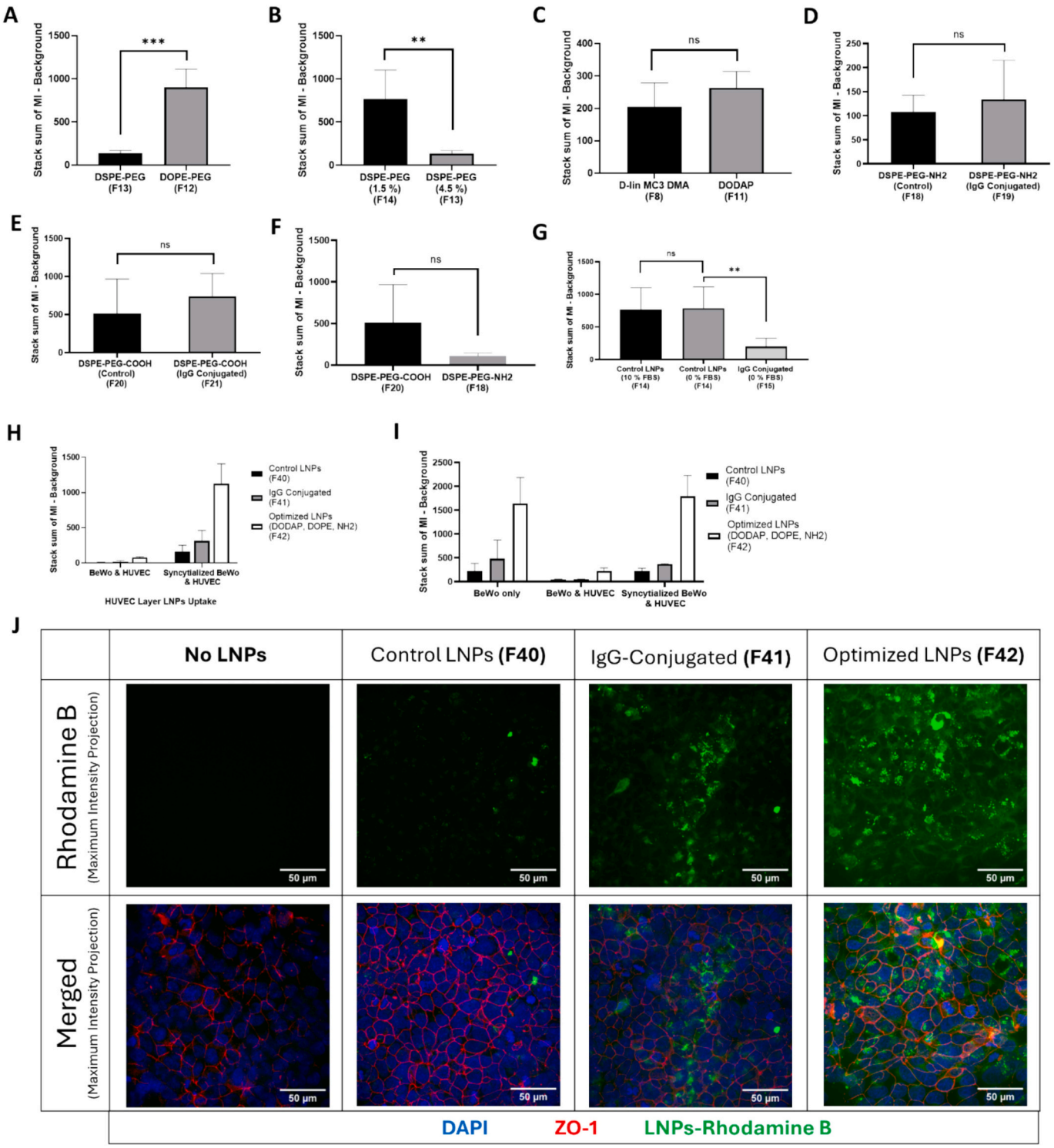

Fig. 8. Cellular association of LNPs with BeWo and HUVEC cells. The effect of (A) PEGylated lipid tail unsaturation, (B) molar percentage of the PEGylated lipid, (C) the ionizable lipid, (D) the PEGylated lipid end-functional group, (E-F) IgG conjugation, (G) percentage FBS concentration in culture media on LNPs association with BeWo cells. Association of different LNPs formulations with (H) HUVEC and (I) BeWo cells in the different placental models. (J) Representative images for cellular association of different LNPs with BeWo cells. Please refer to the Supplementary Table 2 for the detailed description of the LNPs composition and the physicochemical characteristics of each formulation.

can't be generalized to other nanoparticles, but it is specific to our dataset. In our dataset, LNPs with bigger sizes are IgG-conjugated LNPs, while LNPs with high PEGylated lipid percentage have smaller sizes. Also as shown in Fig. 1F, the number of IgG antibodies per LNP was the most critical contributor to LNPs size, and the size increased with a higher number of antibodies per LNP. Finally, the number of LNPs per cell and the mass of LNPs per cell emerged as the second and fourth predictors for transport, respectively. This finding should be considered in dose choices for future studies developing fetal gene therapies or toxicological studies assessing environmental exposure to nanoparticles.

Additionally, we presented the transport data as the average apparent permeability, as described in the methods. This dataset was

modeled for this output and is shown in Supplementary Fig. 6. Since the average apparent permeability calculations considered earlier time points, not just at 24 h, the top predictors in both models were similar but appeared in a different order. LNPs size was shown as the best predictor for permeability while the zeta potential of LNPs was shown to be the second most influential feature.

To better understand the transport process, we studied the kinetics of transport of LNPs by tracking them at several time points up to 24 h. The transport data fit the best to the logistic growth model, which showed lower errors (higher R [2]) compared to other tested kinetics models. From the refined transport dataset, a total of 44 experiments followed the logistic growth model enabling us to calculate k and t-half. The parameter k stands for the rate constant of transport, while t-half represents the time, in hours, to reach half of the maximum concentration. Also, t-half stands for the inflection point where the growth rate is maximal. The ML models were trained on these transport kinetics parameters; the k-values and t-half values serving as the outputs.

SHAP figures were created for k and t-half, as shown in Fig. 6C and D, respectively. From the logistic growth model equation (eq: 4), the k values were inversely proportional to the t-half values. Therefore, the impact of an input feature can have an opposite effect on these two outputs. The LNPs size and zeta potential were among the top five predictors in both models, suggesting their predominant effect on transport kinetics.

Interestingly, the molar percentage of the PEGylated lipids appeared as one of the important features for predicting t-half (Fig. 6D). As the molar percentage of the PEGylated lipids increases, the time required to reach half of the maximum concentration also increases. This new finding emphasizes the critical role of the dePEGylation step to facilitate transport across the placental barrier.

Another interesting result from the k model (Fig. 6C) is that the number of particles per cell was the most important feature for predicting the rate constant of transport, while the mass of LNPs per cell had little to no effect. Even though both represent the dose of LNPs, the number of particles was more predictive of the biological effects. It demonstrated the importance of reporting the dose of nanoparticles as an absolute number concentration. Ouyang et al. have similarly reported the significance of the absolute number concentration of nanoparticles to achieve targeting, demonstrating that a minimum threshold of one trillion nanoparticles per mouse is required to enhance non-liver targeting [71]. With the increasing adoption of counting techniques, such as the nanoparticle tracking analysis (NTA), we anticipate broader adoption among researchers to consistently report the absolute number concentration of nanoparticles in their dosages. This practice will significantly improve future studies on the interaction of nanoparticles with the placenta and other biological barriers by providing accurate and precise number concentration data of nanoparticles.

To validate the effects of these features on LNPs transport, we developed new LNP formulations informed by SHAP analysis. These LNPs were purposefully designed to vary across the different levels of the most important features for predicting LNPs transport at 24 h, namely the zeta potential, number of LNPs per cell, LNPs size, mass of LNPs per cell, and PEGylated lipid end-functional group. Specifically, as shown in Fig. 7A, F49 represented the unoptimized formulation, F50 was moderately optimized by manipulating three features, while F51 was highly optimized by manipulating the five features. We observed a compelling result where combining these features resulted in a synergistic effect on facilitating the transplacental transport of LNPs. As shown in Fig. 7A, the moderately optimized F50 led to a 129 % increase in transport. Remarkably, the highly optimized F51 resulted in a 622 % increase in LNPs transport across the placenta. To improve our understanding of this synergistic effect, we studied the cellular association of LNPs with the placental barrier. We observed a statistically significant increase in cellular association of LNPs by 23 times and 44 times for F50 and F51, respectively, as shown in Fig. 7B. This suggests that the transport process of these optimized LNPs could be mediated by an initial step of placental uptake.

In conclusion, our comprehensive approach combining ML with experimental validation has provided deep insights into the complex dynamics of LNPs transport across the placental barrier. This integrated approach revealed distinctions between interpretations derived from the ML approach in Fig. 6 and conclusions drawn from the traditional single-cause effect testing approach followed in Fig. 4 and Fig. 5. Using ML, we identified critical predictors such as zeta potential, LNPs size, and specific lipid compositions. We have not only refined our understanding of transport kinetics but also highlighted new strategies to optimize LNPs formulations.

3.6. Placental cell association of LNPs

To fully understand the transport mechanism of LNPs across the placental barrier, we conducted a comprehensive cell association study. While measuring transport alone defines LNPs crossing the placenta, it does not account for the complex interactions between LNPs and placental cells. By quantifying cellular association, encompassing both uptake and adhesion to cells, we can better interpret transport results and identify the underlying mechanisms driving LNPs behavior. We used fluorescence imaging to measure cell association of LNPs following 24 h transport and *Z*-stacks were quantified for fluorescence intensity. The sum of the mean fluorescence intensity of each slice was used for comparing the different experiments.

Aligned with transport results (Fig. 4), PEGylated lipid tail saturation and PEGylated lipid percentage were determinants of cellular association, where higher cellular association of LNPs were observed for DOPE-PEG versus DSPE-PEG containing LNPs (Fig. 8A). Also, as we increased the molar percentage of DSPE-PEG a significant decrease in cellular association was observed. Therefore, faster dePEGylation (or PEGylated lipid dissociation) could be a crucial step for association of LNPs with trophoblasts (Fig. 8B). These transport and cellular association studies on the effect of PEGylated lipid on LNPs behavior corroborate previous studies assessing nanoparticle uptake and biodistribution [61,72]. The same was observed for the features, ionizable lipid type and IgG conjugation, however the difference in cellular association was not statistically significant (Fig. 8C-E). Overall, these data suggest that cell uptake for these LNPs could be a prerequisite for successful transport across the placental barrier. The lack of significance in cellular association could be due to the sensitivity limitations of image analysis based on fluorescence intensity, as we reported earlier [73,74]. Another method that compares the number of fluorescent voxels, outlined in Supplementary Fig. 8, could provide more information.

Interestingly, the cellular association results further strengthen our hypothesis regarding the increased cell permeability upon induction of syncytialization by forskolin. Specifically, a significant increase in LNPs association to both placental and endothelial cells was observed following induction of syncytialization, as seen in Fig. 8I and H. This aligns with the concomitant increase in transport observed in Fig. 5C.

On the contrary, varying the PEGylated lipid end-functional group did not result in significant changes in cellular association of LNPs. This is despite the difference in transport observed between the LNPs with DSPE-PEG-COOH and DSPE-PEG-NH2. Also, we observed a reduction in cellular association of IgG-conjugated LNPs when dispersed in IgG-deprived media (0 % FBS), as shown in Fig. 8G, despite the high percentage transport of this formulation (Fig. 5B). The underlying mechanisms for these observations remain unclear and warrant further investigation. One suggestion is that the end-functional group and IgG concentration in the media played a critical role in transport but were not required for initial cellular association.

In conclusion, understanding the cellular association of LNPs provides valuable insights into their transport behavior across the placental barrier and highlights the complex interplay of lipid composition and cellular interactions.

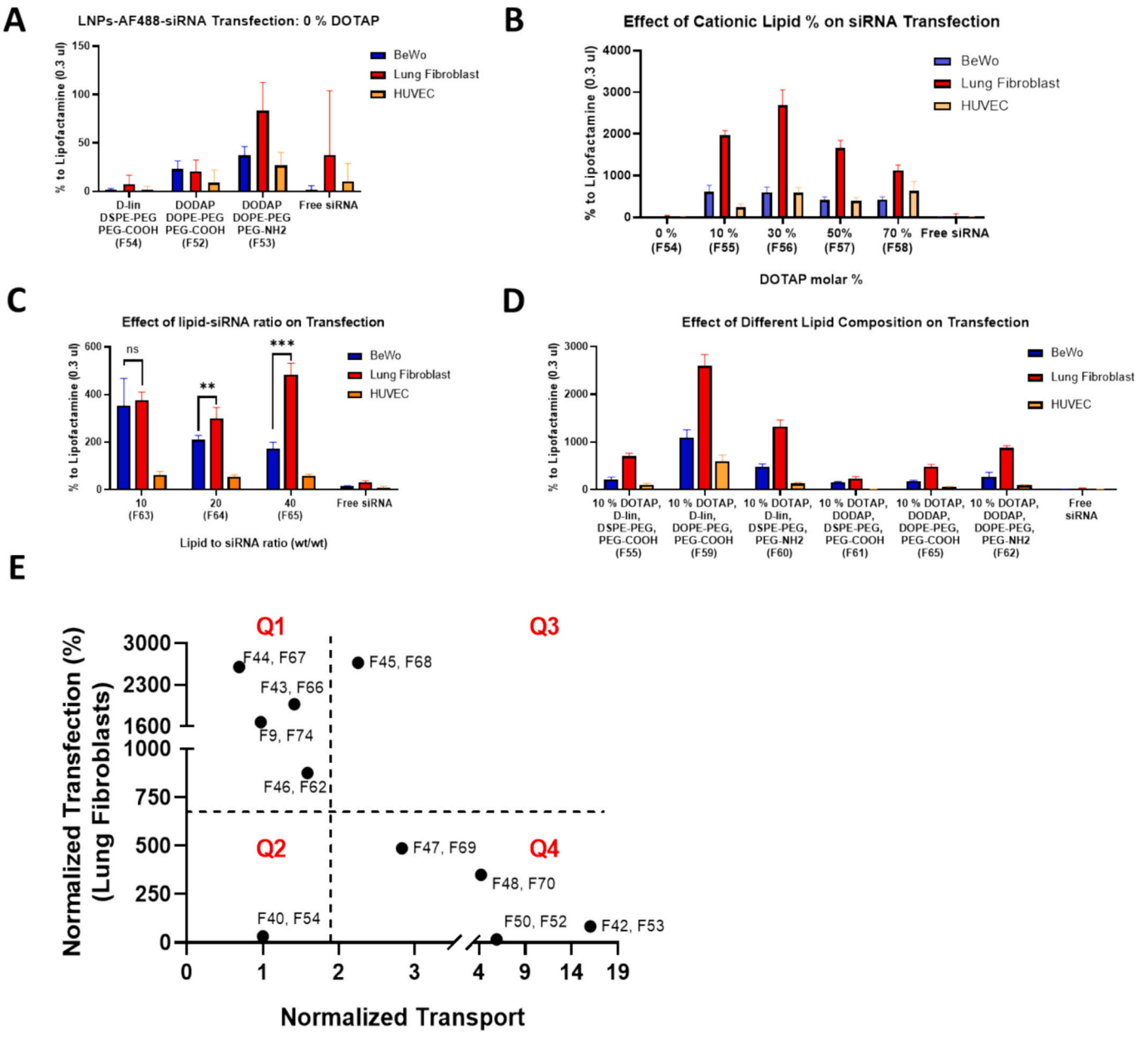

Fig. 9. Transfection of siRNA-loaded LNPs in placental and fetal cells is derived by cationic lipids, PEGylated lipids, and lipid to siRNA ratio. (A) Transfection of high-transport formulations that do not include DOTAP in their lipid composition. (B) The effect of DOTAP molar percentage on percentage transfection. (C) Effect of lipid to siRNA mass ratio on percentage transfection. (D) Optimizing formulations for high transport and high transfection by testing different compositions with lipids identified for increasing the transport. (E) The placental transport and lung fibroblasts transfection results combined; each dot represents LNPs with the same lipid composition but with 2 IDs: the first one is unloaded LNPs used for the transport experiment and the second one is siRNA-loaded LNPs tested for transfection. The dashed lines represent the median of the output and divide the performance of the formulations into 4 quadrants: Q1 is low transport & high transfection, Q2 is low transport & low transfection, Q3 is high transport & high transfection, and Q4 is high transport & low transfection. Please refer to the Supplementary Table 2 for the detailed description of the LNPs composition and the physicochemical characteristics of each formulation. Transfection results are reported as a percentage relative to the positive control (which is transfection by Lipofectamine).

3.7. siRNA-loaded LNPs transfection in placental and fetal cells

To build on the findings from our transport study, we initiated an in vitro transfection study to further optimize LNPs formulations for RNA delivery to human fetal lung fibroblasts. Our goal was to develop siRNA-loaded LNPs formulations that preferentially transfect fetal lung cells while minimizing transfection in off-target placental or endothelial cells.

This study also addresses a current gap in knowledge. Previous studies attempted to optimize LNPs to achieve mRNA transfection in the placental cells [75,76], or in fetal cells through intraamniotic injection, vitelline vein injection, or intracerebroventricular injection [4,77]. However, developing an LNP formulation that preferentially transfects fetal lung cells over placental or endothelial cells requires further optimization.

When we tested the high placental transport formulations, that included two or three of these lipids: DODAP, DOPE-PEG, and DSPE-PEG-NH2, they showed a slight increase in transfection. However, the overall efficiency was comparable to free siRNA using lipofactamine, as shown in Fig. 9A. Therefore, we conducted several optimizations to improve relative transfection efficiency in fetal lung fibroblast cells to placental cells and endothelial cells.

First, we tested different LNPs to siRNA mass ratios. A mass ratio of

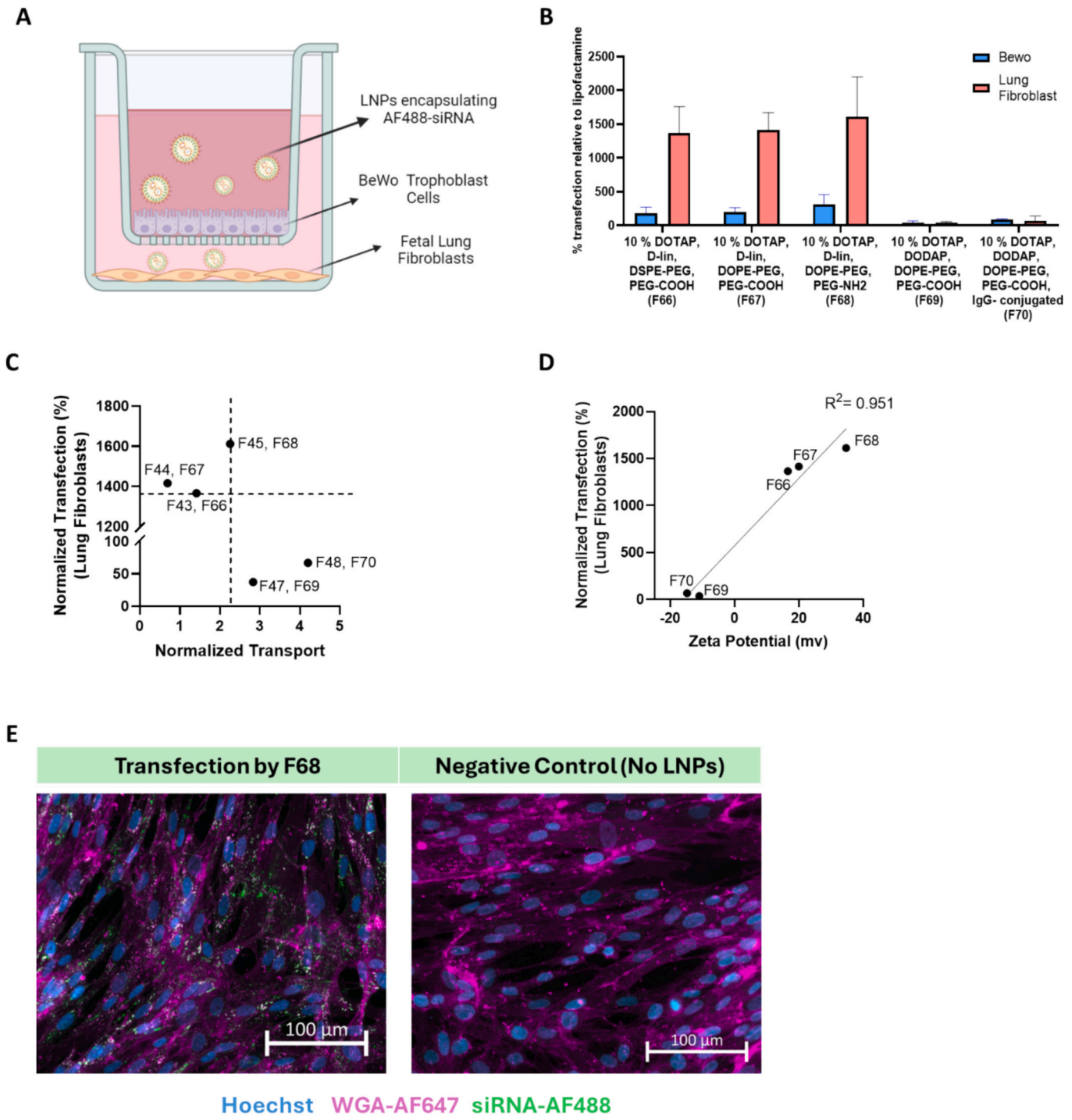

Fig. 10. Combined Transport-Transfection Model. (A) A Schematic for the combined model with BeWo cells seeded on the transwell membrane in the apical compartment and fetal lung fibroblasts on the bottom of the basolateral compartment; Created with BioRender.com. (B) siRNA transfection in BeWo cells and lung fibroblasts using the combined model. (C) The formulations represented by their transport and lung fibroblast transfection results combined; the dashed lines represent the median of the two outputs. (D) The relationship between zeta potential and lung fibroblasts transfection in the combined model. (E) Representative image for siRNA transfection into lung fibroblasts using the combined model by formulation no 68. Please refer to the Supplementary Table 2 for the detailed description of the LNPs composition and the physicochemical characteristics of each formulation.

40 (formulation 65) showed significant transfection in lung cells compared to placental cells, while a mass ratio of 10 (formulation 63) showed no differences, as shown in Fig. 9C. Therefore, the ratio of 40 was utilized for all subsequent formulations. This confirms previous studies that showed that increasing the N/P ratio (the ratio between lipid and RNA) results in preferential transfection of the lung cells [78].

To further increase the transfection percentage in lung cells, LNPs with different molar percentages of DOTAP were tested. Recent studies have shown that permanent cationic lipids, such as DOTAP, can increase mRNA transfection into lung cells as they raise the LNPs pKa above 7 [66]. As shown in Fig. 9B, DOTAP molar percentages of 10 and 30 achieved the highest transfection percentage in fetal lung cells. However, increasing the DOTAP percentage beyond this resulted in a reduction in the number of viable cells. Therefore, the 10 % DOTAP was

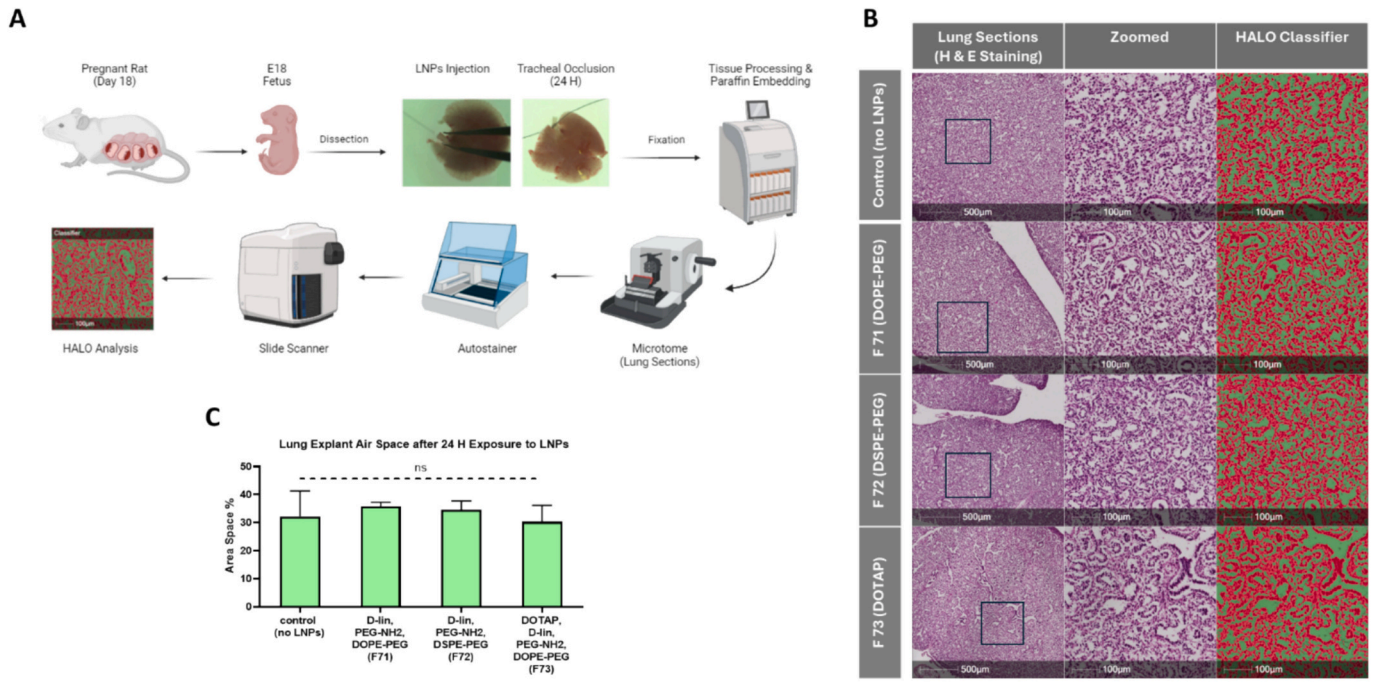

Fig. 11. Ex vivo testing of the safety of LNPs in fetal lung explants. (A) The lung explant LNPs testing workflow;Created with BioRender.com. (B) Representative images for Hematoxylin and Eosin (H&E) staining after 24 h exposure to different LNPs; the black box in each image outlines the zoomed-in part. HALO classifier shows what represents the airspaces (in green) and the lung tissue (in red). (C) The lung air space after 24 h exposure to different LNPs. Please refer to the Supplementary Table 2 for the detailed description of the LNPs composition and the physicochemical characteristics of each formulation. (For interpretation of the references to color in this figure legend, the reader is referred to the web version of this article.)

included in subsequent formulations to achieve high transfection while keeping high molar percentages of the other lipids driving transport.

Following determination of the optimal DOTAP molar percentage of 10 and the optimal LNPs to siRNA mass ratio of 40, we tested the impact of other lipid components shown to drive high placental transport, on transfection efficiency. Similar to the transport results, replacing DSPE-PEG-COOH with DSPE-PEG-NH2, or replacing DSPE-PEG with DOPE-PEG resulted in a significant increase in transfection, mainly due to the increase in zeta potential or more rapid de-PEGylation [61], respectively (Fig. 9D). However, contrary to the transport results, replacing D-lin-MC3 with DODAP led to a significant reduction in transfection. Therefore, the lipids driving high placental transport are not necessarily the same ones leading to high fetal cell transfection. So, a balance between both is required. It should be also noted that these transfection experiments were conducted at a dose of 4 picomole siRNA per well (0.35 cm^2). To investigate the impact of siRNA dose on transfection efficiency, we tested a smaller dose of one picomole of siRNA per well (Supplementary Fig. 7). Similar transfection results were obtained indicating that the behavior of LNPs can be dose independent.

The ten LNPs formulations tested separately for placental transport and fetal lung transfection were plotted based on their measured 24-h transport and transfection results (Fig. 9F). The median for the two outputs (transport and transfection) was graphed dividing the overall output of the LNPs formulations into four quadrants: Q1 (high transfection and low transport), Q2 (low transfection and low transport), Q3 (high transfection and high transport) and Q4 (low transfection and high transport). Among the different formulations, F68 composed of (DOTAP, D-lin MC3, cholesterol, DSPC, DOPE-PEG, and DSPE-PEG-NH2) were shown to efficiently cross the placental barrier and to transfect fetal lung cells.

3.8. Combined transport-transfection study

Formulations representing the different quadrants (Q1, Q2, Q3 and Q4 - Fig. 9F) were tested in a combined transport and transfection placental model shown in Fig. 10A. The use of this model confirms if LNPs are intact and capable of transfecting fetal lung cells after passing through the placental barrier. A similar high-throughput set-up to test the LNPs integrity was utilized in a previous study modeling the blood-brain barrier [42].

All of the tested LNPs formulations included 10 % DOTAP, shown to induce high transfection efficiency (Fig. 9B-D) in addition to the lipid composition of LNPs formulations with high transport features. Among these tested formulations, LNPs containing D-lin MC3 showed significantly higher fetal lung fibroblast transfection compared to the ones containing DODAP (Fig. 10B). This could be explained by the high correlation ($R^2 = 0.95$) that was found between zeta potential and fetal lung fibroblast transfection in the combined model (Fig. 10D). Fig. 10E shows transfected fetal lung fibroblasts using Formulation 68, which has achieved the synergy between high transport and transfection efficiencies (Fig. 10C) and has the highest zeta potential.

3.9. Ex vivo screening of lipid nanoparticle safety on fetal lungs

Previous studies targeting the placenta showed no fetal exposure to the nanoparticles and no effect on fetal outcome [76,79]. However, a recent study showed that even if there was no direct fetal exposure, nanoparticles still pose a risk for fetal development as they can disrupt the placental secretome [80]. In addition, recent efforts for fetal gene therapies have recommended direct injection to the fetus through the amniotic sac or the fetal vitelline vein, which leads to NP exposure in the different fetal organs, such as the lungs or liver [77,81].

Abnormal lung development as observed in congenital diaphragmatic hernia (CDH) is one of the deadliest fetal anomalies [5]. Thus, targeting the abnormal lungs with a specific genetic modality could offer cures for deadly diseases [5]. Therefore, it is essential to investigate the toxicity of different LNPs compositions on lung development to guide future studies on targeted fetal gene therapies. Hence, in this study, a fetal lung explant model was used to assess the outcomes from direct exposure to different LNPs of varying composition, as outlined in Fig. 11.

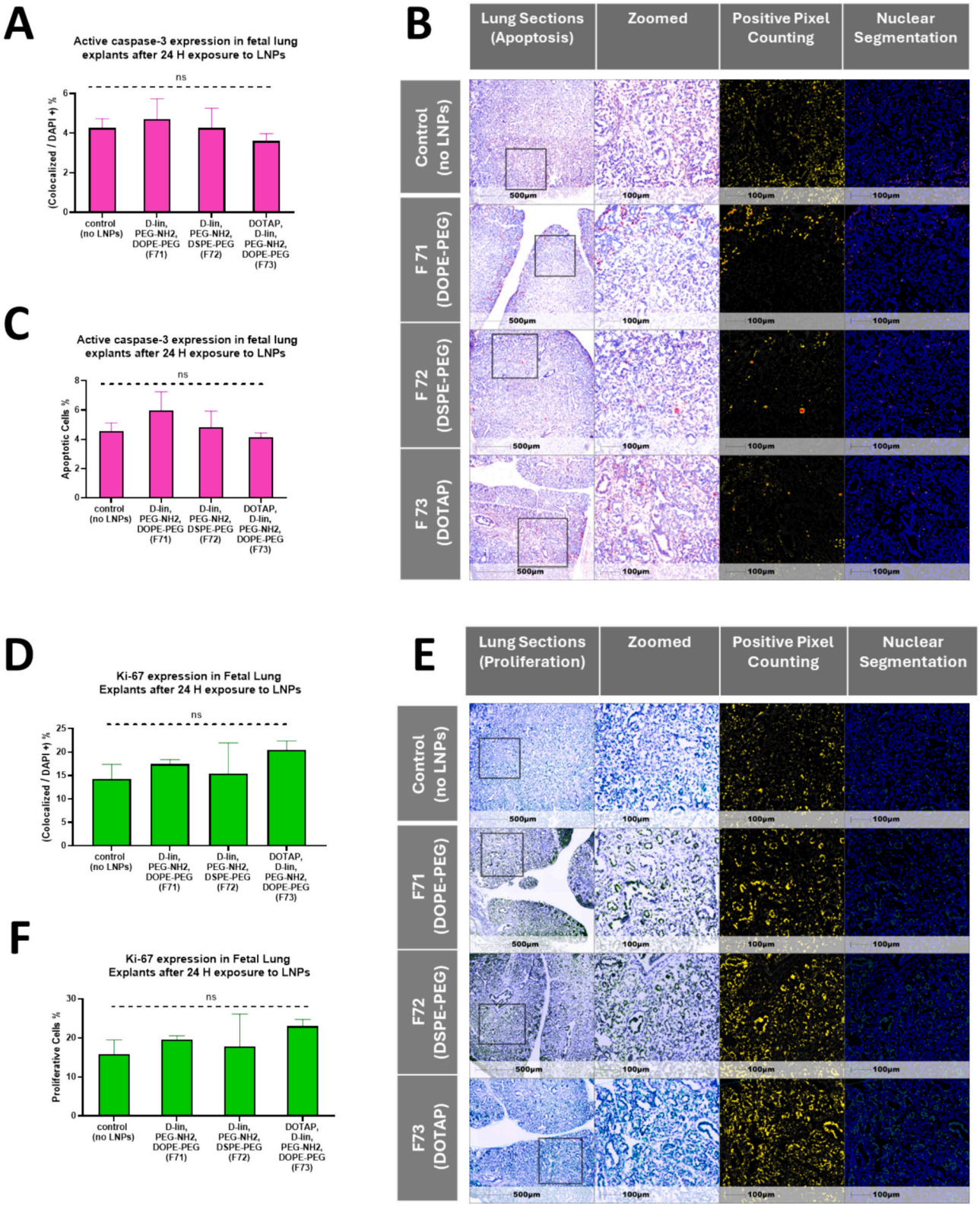

Fig. 12. Immunofluorescence staining for apoptosis and proliferation in the fetal lung explant. Staining signal of the different LNPs groups using the positive pixel counting analysis method, by dividing the colocalized signal over the DAPI+ signal: (A) Active Caspase-3, (D) ki-67. Staining signal of the different LNPs groups using the nuclear segmentation method to count the number of cells: (C) Active Caspase-3, (F) ki-67. Representative images of the immunostaining: (B) Active Caspase-3, (E) ki-67; black boxes outline the zoomed-In part; Positive pixel counting images display the pixels that exceed the minimum threshold (in yellow); the nuclear segmentation images show the apoptotic cells (in purple), and proliferative cells (in green). (For interpretation of the references to color in this figure legend, the reader is referred to the web version of this article.)

Evaluating the air spaces of the lung has been used as a surrogate marker to study normal lung development and compare it to diseased states [27]. In the current study, the Autostainer, Slide Scanner, and HALO analysis have been used to automate the workflow of histological studies, as shown in Fig. 11. Image analysis of H&E stained sections showed no effect on the lung airspace composition in the different LNPs groups compared to the control group, as shown in Fig. 11C.

Apoptosis is considered a hallmark of normal lung development [27]. However, excessive exposure to nanoparticles could lead to higher apoptosis. Since Caspase-3 and Caspase-9 are considered central regulators of apoptosis [82], their abundance were evaluated as surrogate marker of the apoptosis. Previous studies showed that cationic lipids' headgroups structure could induce cytotoxic behavior through a caspase-dependent mitochondrial intrinsic pathway [83]. Following 24 h of exposure to different LNPs, there was no significant difference in Active Caspase-3 abundance between the different LNPs formulations and the control group, as shown in Fig. 12A-C. The analysis was performed using the positive pixel counting and nuclear segmentation methods available in HALO software, as shown in Fig. 12A and B.

In addition, fetal lung proliferation is highly active at this stage of development. Ki-67 abundance, which marks proliferative cells, was not affected by the exposure to different LNPs (Fig. 12 D—F).

These findings support the feasibility of exploring LNPs for targeted fetal gene therapies aimed at addressing lethal fetal anomalies, such as CDH, while emphasizing the importance of continued safety assessments in future studies.

4. Conclusion

In this work, we developed a library of diverse LNPs by varying the types and ratios of the different lipid classes. Using this library, we took two approaches to study the placental transport of LNPs: statistical analysis and machine learning. Statistical analysis has identified key parameters influencing the transport, such as the antibody conjugation mechanism and the PEGylated lipid's percentage, tail saturation, and end-functional group. However, the ML model identified more properties driving the transport, such as the zeta potential, size, and concentration. Relying on the ML model results, we further optimized the LNPs formulation to include properties and compositions that induce transport. We were able to purposely design formulations that had low, medium, or high placental transport. These results are of significance for future studies aiming at developing LNPs formulation targeting maternal organs (requiring low placental transport) or fetal organs (requiring high transplacental transport).

However, a limitation of our developed ML models is their reliance on a relatively small dataset, derived from a single study, compared to larger datasets encompassing multiple studies. We are sharing our dataset (Supplementary file 3). So that additional data points from future studies can be incorporated, particularly considering the ongoing development of new lipids and other nanocarriers. This will accelerate the development of validated LNPs properties and transport results, thus fostering collaboration and advancing research on NP interactions with the placenta.

Combining the transport and cellular association studies has depicted the importance of the placental model structure and the dePEGylation step in influencing the uptake and transport of LNPs. Besides, the transfection studies have confirmed the importance of cationic lipids and N/P ratio in the preferential transfection of lung cells. Studying the LNPs in the combined transport and transfection model has shown that LNPs could bypass the placental barrier and transfect fetal cells, which could be a potential route to reach fetal organs. However, this could also raise concerns about environmental exposure to different NPs during pregnancy.

Finally, our ex vivo results suggest the safety of LNPs during fetal organ development that enable their use as a safe gene delivery vehicle during pregnancy. However, our in vitro viability studies raise concerns about incorporating high concentrations of permanently cationic lipids, which have been followed in different studies targeting the lung. Future studies should focus on the development of other safe ionizable lipids that can target the fetal lung and other fetal organs.

CRediT authorship contribution statement

Amr Abostait: Writing – review & editing, Writing – original draft, Visualization, Validation, Software, Methodology, Investigation, Formal analysis, Data curation, Conceptualization. **Mahmoud Abdelkarim:** Writing – review & editing, Visualization, Validation, Methodology, Investigation, Formal analysis, Data curation, Conceptualization. **Zeqing Bao:** Writing – review & editing, Visualization, Validation, Methodology, Investigation, Formal analysis, Data curation. **Yuichiro Miyake:** Writing – review & editing, Methodology, Investigation. **Wai Hei Tse:** Writing – review & editing, Methodology, Investigation, Conceptualization. **Caterina Di Ciano-Oliveir:** Writing – review & editing, Methodology, Investigation, Formal analysis. **Tina Buerki-Thurnherr:** Writing – review & editing, Resources, Methodology. **Christine Allen:** Writing – review & editing, Visualization, Validation, Methodology, Investigation, Formal analysis, Data curation. **Richard Keijzer:** Writing – review & editing, Supervision, Funding acquisition, Conceptualization. **Hagar I. Labouta:** Writing – review & editing, Visualization, Validation, Supervision, Software, Resources, Project administration, Methodology, Investigation, Funding acquisition, Formal analysis, Data curation, Conceptualization.

Declaration of competing interest

None.

Data availability

Data will be made available on request.

Acknowledgement

We want to thank Mr. Daywin Patel and Dr. Arzu Ozturk from the Children's Hospital Research Institute of Manitoba, and Mr. Xiaofeng Lu from the core facilities at St. Michael's Hospital for their support in the animal work and histological studies. Biorender and GraphPad Prism were used to create the figures.

We also acknowledge the financial support by New Frontiers Research Fund – Exploration Grant NFRFE-2019-00210), SickKids Foundation in partnership with the Canadian Institutes of Health Research (NI22-1088R), and the Natural Sciences and Engineering Research Council (NSERC Discovery Grant-RGPIN-2020-05679 and NSERC RTI-2021-00374). A.A. was supported by Research Manitoba Master Studentship, Rady Faculty of Health Sciences Master Studentship, and Women's Health Research Foundation of Canada Scholarship. M. A. is supported by Lloyd and Marie Barbara PhD Scholarship from St. Michael's Hospital Foundation. R.K. is the inaugural Thorlakson Chair in Surgical Research for the University of Manitoba and parts of this work were supported by an operating grant from the Children's Hospital Research Institute of Manitoba.

Appendix A. Supplementary data

Supplementary data to this article can be found online at https://doi.org/10.1016/j.jconrel.2024.10.047.

References

[1] R. Palanki, W.H. Peranteau, M.J. Mitchell, Delivery technologies for in utero gene therapy, Adv. Drug Deliv. Rev. 169 (2021) 51–62.
[2] P.S. Puligandla, E.D. Skarsgard, The Canadian pediatric surgery network congenital diaphragmatic hernia evidence review project: developing national guidelines for care, Paediatr. Child Health 21 (4) (2016) 183–186.
[3] L. Yu, R.R. Hernan, J. Wynn, W.K. Chung, The influence of genetics in congenital diaphragmatic hernia, Semin. Perinatol. 44 (1) (2020) 151169.
[4] R. Palanki, S.K. Bose, A. Dave, et al., Ionizable lipid nanoparticles for therapeutic base editing of congenital brain disease, ACS Nano 17 (14) (2023) 13594–13610.
[5] N. Khoshgoo, R. Kholdebarin, P. Pereira-Terra, et al., Prenatal microRNA miR-200b therapy improves nitrofen-induced pulmonary hypoplasia associated with congenital diaphragmatic hernia, Ann. Surg. 269 (5) (2019) 979–987.
[6] J.S. Amberger, C.A. Bocchini, A.F. Scott, A. Hamosh, OMIM.org: leveraging knowledge across phenotype-gene relationships, Nucleic Acids Res. 47 (D1) (2019) D1038–D1043.
[7] P.D. Robbins, S.C. Ghivizzani, Viral vectors for gene therapy, Pharmacol. Ther. 80 (1) (1998) 35–47.
[8] T. Dobrowsky, D. Gianni, J. Pieracci, J. Suh, AAV manufacturing for clinical use: insights on current challenges from the upstream process perspective, Curr. Opin. Biomed. Eng. (2021) 20.
[9] J.L. Shirley, Y.P. de Jong, C. Terhorst, R.W. Herzog, Immune responses to viral gene therapy vectors, Mol. Ther. 28 (3) (2020) 709–722.
[10] K. Paunovska, D. Loughrey, J.E. Dahlman, Drug delivery systems for RNA therapeutics, Nat. Rev. Genet. 23 (5) (2022) 265–280.
[11] S. Ren, M. Wang, C. Wang, et al., Application of non-viral vectors in drug delivery and gene therapy, Polymers (Basel) 13 (19) (2021).
[12] C. Hald Albertsen, J.A. Kulkarni, D. Witzigmann, M. Lind, K. Petersson, J. B. Simonsen, The role of lipid components in lipid nanoparticles for vaccines and gene therapy, Adv. Drug Deliv. Rev. 188 (2022) 114416.
[13] V. Patel, R. Lalani, D. Bardoliwala, S. Ghosh, A. Misra, Lipid-based oral formulation strategies for lipophilic drugs, AAPS PharmSciTech 19 (8) (2018) 3609–3630.
[14] M. Schlich, R. Palomba, G. Costabile, et al., Cytosolic delivery of nucleic acids: the case of ionizable lipid nanoparticles, Bioeng. Transl. Med. 6 (2) (2021) e10213.
[15] A. Akinc, M.A. Maier, M. Manoharan, et al., The Onpattro story and the clinical translation of nanomedicines containing nucleic acid-based drugs, Nat. Nanotechnol. 14 (12) (2019) 1084–1087.
[16] L. Schoenmaker, D. Witzigmann, J.A. Kulkarni, et al., mRNA-lipid nanoparticle COVID-19 vaccines: structure and stability, Int. J. Pharm. 601 (2021) 120586.
[17] W.H. Tse, S. Higgins, D. Patel, et al., The maternal-fetal transfer of passive immunity as a mechanism of transplacental nanoparticle drug delivery for prenatal therapies, Biomater. Sci. 10 (18) (2022) 5243–5253.
[18] R. Bajoria, S.F. Contractor, Effect of the size of liposomes on the transfer and uptake of carboxyfluorescein by the perfused human term placenta, J. Pharm. Pharmacol. 49 (7) (1997) 675–681.
[19] L. Aengenheister, B.B. Dugershaw, P. Manser, et al., Investigating the accumulation and translocation of titanium dioxide nanoparticles with different surface modifications in static and dynamic human placental transfer models, Eur. J. Pharm. Biopharm. 142 (2019) 488–497.
[20] H. Yang, C. Sun, Z. Fan, et al., Effects of gestational age and surface modification on materno-fetal transfer of nanoparticles in murine pregnancy, Sci. Rep. 2 (2012) 847.
[21] L. Aengenheister, R.R. Favaro, D.M. Morales-Prieto, et al., Research on nanoparticles in human perfused placenta: state of the art and perspectives, Placenta 104 (2021) 199–207.
[22] Z. Bao, J. Bufton, R.J. Hickman, A. Aspuru-Guzik, P. Bannigan, C. Allen, Revolutionizing drug formulation development: the increasing impact of machine learning, Adv. Drug Deliv. Rev. 202 (2023) 115108.
[23] Z. Bao, F. Yung, R.J. Hickman, A. Aspuru-Guzik, P. Bannigan, C. Allen, Data-driven development of an oral lipid-based nanoparticle formulation of a hydrophobic drug, Drug Deliv. Transl. Res. 14 (7) (2024) 1872–1887.
[24] B.B. Dugershaw, L. Aengenheister, S.S.K. Hansen, K.S. Hougaard, T. Buerki-Thurnherr, Recent insights on indirect mechanisms in developmental toxicity of nanomaterials, Part. Fibre Toxicol. 17 (1) (2020) 31.
[25] H.I. Labouta, C. Sarsons, J. Kennard, et al., Understanding and improving assays for cytotoxicity of nanoparticles: what really matters? RSC Adv. 8 (41) (2018) 23027–23039.
[26] S.H. Mostafaei, J. Tanha, OUBoost: boosting based over and under sampling technique for handling imbalanced data, Int. J. Mach. Learn. Cybern. 14 (10) (2023) 3393–3411.
[27] Y. Miyake, W.H. Tse, J.Q. Wang, et al., The effect of tracheal occlusion in congenital diaphragmatic hernia in the nitrofen rat lung explant model, Pediatr. Surg. Int. 39 (1) (2022) 61.
[28] Y. Miyake, W.H. Tse, J.Q. Wang, et al., Microinjection with nanoparticles to deliver drugs in prenatal lung explants - a pilot study for prenatal therapy in congenital diaphragmatic hernia, J. Pediatr. Surg. 59 (5) (2024) 847–853.
[29] M.S. Ali, N. Hooshmand, M. El-Sayed, H.I. Labouta, Microfluidics for development of lipid nanoparticles: paving the way for nucleic acids to the clinic, ACS Appl. Bio Mater. 6 (9) (2023) 3566–3576.
[30] X. Chen, H. Lv, Intelligent control of nanoparticle synthesis on microfluidic chips with machine learning, NPG Asia Mater. 14 (1) (2022) 69.
[31] J.A. Kulkarni, D. Witzigmann, J. Leung, Y.Y.C. Tam, P.R. Cullis, On the role of helper lipids in lipid nanoparticle formulations of siRNA, Nanoscale 11 (45) (2019) 21733–21739.
[32] H.C. Geisler, A.A. Ghalsasi, H.C. Safford, et al., EGFR-targeted ionizable lipid nanoparticles enhance in vivo mRNA delivery to the placenta, J. Control. Release 371 (2024) 455–469.
[33] Z.R. Cohen, S. Ramishetti, N. Peshes-Yaloz, et al., Localized RNAi therapeutics of chemoresistant grade IV glioma using hyaluronan-grafted lipid-based nanoparticles, ACS Nano 9 (2) (2015) 1581–1591.
[34] S. Ramishetti, R. Kedmi, M. Goldsmith, et al., Systemic gene silencing in primary T lymphocytes using targeted lipid nanoparticles, ACS Nano 9 (7) (2015) 6706–6716.
[35] S.M. Lundberg, G. Erion, H. Chen, et al., From local explanations to global understanding with explainable AI for trees, Nat. Mach. Intell. 2 (1) (2020) 56–67.
[36] C.G. Figueroa-Espada, S. Hofbauer, M.J. Mitchell, R.S. Riley, Exploiting the placenta for nanoparticle-mediated drug delivery during pregnancy, Adv. Drug Deliv. Rev. 160 (2020) 244–261.
[37] Z. Zhou, D. Luo, M. Li, et al., A novel multicellular placental barrier model to investigate the effect of maternal aflatoxin B, Toxins (Basel) 15 (5) (2023).
[38] S. Kouthouridis, A. Sotra, Z. Khan, J. Alvarado, S. Raha, B. Zhang, Modeling the progression of placental transport from early- to late-stage pregnancy by tuning trophoblast differentiation and vascularization, Adv. Healthc. Mater. 12 (32) (2023) e2301428.
[39] X. Huang, M. Lüthi, E.C. Ontsouka, et al., Establishment of a confluent monolayer model with human primary trophoblast cells: novel insights into placental glucose transport, Mol. Hum. Reprod. 22 (6) (2016) 442–456.
[40] L. Aengenheister, K. Keevend, C. Muoth, et al., An advanced human in vitro co-culture model for translocation studies across the placental barrier, Sci. Rep. 8 (1) (2018) 5388.
[41] M.K. Wong, E.W. Li, M. Adam, P.R. Selvaganapathy, S. Raha, Establishment of an in vitro placental barrier model cultured under physiologically relevant oxygen levels, Mol. Hum. Reprod. 26 (5) (2020) 353–365.
[42] E.L. Han, M.S. Padilla, R. Palanki, et al., Predictive high-throughput platform for dual screening of mRNA lipid nanoparticle blood-brain barrier transfection and crossing, Nano Lett. 24 (5) (2024) 1477–1486.
[43] A. Abostait, J. Tyrrell, M. Abdelkarim, et al., Placental nanoparticle uptake-on-a-chip: the impact of trophoblast syncytialization and shear stress, Mol. Pharm. 19 (11) (2022) 3757–3769.
[44] D.E. Vaughn, P.J. Bjorkman, Structural basis of pH-dependent antibody binding by the neonatal fc receptor, Structure 6 (1) (1998) 63–73.
[45] T. Clements, T.F. Rice, G. Vamvakas, et al., Update on transplacental transfer of IgG subclasses: impact of maternal and fetal factors, Front. Immunol. 11 (2020) 1920.
[46] H.I. Labouta, S. Menina, A. Kochut, et al., Bacteriomimetic invasin-functionalized nanocarriers for intracellular delivery, J. Control. Release 220 (2015). Part A:414-424.
[47] S. Wang, X. Wei, X. Sun, et al., A novel therapeutic strategy for cartilage diseases based on lipid nanoparticle-RNAi delivery system, Int. J. Nanomedicine 13 (2018) 617–631.
[48] M.P. Mattson, Hormesis defined, Ageing Res. Rev. 7 (1) (2008) 1–7.
[49] X. Wei, B. Shao, Z. He, et al., Cationic nanocarriers induce cell necrosis through impairment of Na(+)/K(+)-ATPase and cause subsequent inflammatory response, Cell Res. 25 (2) (2015) 237–253.
[50] M.S. Hanafy, H.M. Dao, H. Xu, J.J. Koleng, W. Sakran, Z. Cui, Effect of the amount of cationic lipid used to complex siRNA on the cytotoxicity and proinflammatory activity of siRNA-solid lipid nanoparticles, Int. J. Pharm. X 6 (2023) 100197.
[51] D.R. Martinez, Y. Fong, S.H. Li, et al., Fc characteristics mediate selective placental transfer of IgG in HIV-infected women, Cell 178 (1) (2019) 190–201.e111.
[52] M.M. Gruber, B. Hirschmugl, N. Berger, et al., Plasma proteins facilitates placental transfer of polystyrene particles, J. Nanobiotechnol. 18 (1) (2020) 128.
[53] E.M. Pridgen, F. Alexis, T.T. Kuo, et al., Transepithelial transport of Fc-targeted nanoparticles by the neonatal fc receptor for oral delivery, Sci. Transl. Med. 5 (213) (2013), 213ra167.
[54] L. Ducry, Antibody-Drug Conjugates, Humana Press ; Springer, New York, 2013.
[55] S. Okyem, O. Awotunde, T. Ogunlusi, M.B. Riley, J.D. Driskell, High-affinity points of interaction on antibody allow synthesis of stable and highly functional antibody-gold nanoparticle conjugates, Bioconjug. Chem. 32 (8) (2021) 1753–1762.
[56] R. Jue, J.M. Lambert, L.R. Pierce, R.R. Traut, Addition of sulfhydryl groups to Escherichia coli ribosomes by protein modification with 2-iminothiolane (methyl 4-mercaptobutyrimidate), Biochemistry 17 (25) (1978) 5399–5406.
[57] N. Escareño, N. Hassan, M.J. Kogan, J. Juárez, A. Topete, A. Daneri-Navarro, Microfluidics-assisted conjugation of chitosan-coated polymeric nanoparticles with antibodies: significance in drug release, uptake, and cytotoxicity in breast cancer cells, J. Colloid Interface Sci. 591 (2021) 440–450.
[58] P. Cuatrecasas, I. Parikh, Adsorbents for affinity chromatography. Use of N-hydroxysuccinimide esters of agarose, Biochemistry 11 (12) (1972) 2291–2299.
[59] E.A. Berg, J.B. Fishman, Labeling antibodies, Cold Spring Harb Protoc 2020 (7) (2020) 099242.
[60] A.C. Anselmo, S. Mitragotri, Nanoparticles in the clinic: an update, Bioeng. Transl. Med. 4 (3) (2019) e10143.
[61] X. Zhu, W. Tao, D. Liu, et al., Surface de-PEGylation controls nanoparticle-mediated siRNA delivery, Theranostics 7 (7) (2017) 1990–2002.
[62] L.E. Waggoner, K.F. Miyasaki, E.J. Kwon, Analysis of PEG-lipid anchor length on lipid nanoparticle pharmacokinetics and activity in a mouse model of traumatic brain injury, Biomater. Sci. 11 (12) (2023) 4238–4253.
[63] R.C. Ryals, S. Patel, C. Acosta, M. McKinney, M.E. Pennesi, G. Sahay, The effects of PEGylation on LNP based mRNA delivery to the eye, PLoS One 15 (10) (2020) e0241006.

[64] S. Sabnis, E.S. Kumarasinghe, T. Salerno, et al., A novel amino lipid series for mRNA delivery: improved endosomal escape and sustained pharmacology and safety in non-human primates, Mol. Ther. 26 (6) (2018) 1509–1519.
[65] Q. Cheng, T. Wei, L. Farbiak, L.T. Johnson, S.A. Dilliard, D.J. Siegwart, Selective organ targeting (SORT) nanoparticles for tissue-specific mRNA delivery and CRISPR-Cas gene editing, Nat. Nanotechnol. 15 (4) (2020) 313–320.
[66] S.A. Dilliard, Q. Cheng, D.J. Siegwart, On the mechanism of tissue-specific mRNA delivery by selective organ targeting nanoparticles, Proc. Natl. Acad. Sci. USA 118 (52) (2021).
[67] T. Yue, H. Zhou, H. Sun, et al., Why are nanoparticles trapped at cell junctions when the cell density is high? Nanoscale 11 (14) (2019) 6602–6609.
[68] S.J. Renaud, M.J. Jeyarajah, How trophoblasts fuse: an in-depth look into placental syncytiotrophoblast formation, Cell. Mol. Life Sci. 79 (8) (2022) 433.
[69] B. Zhang, R. Liang, M. Zheng, L. Cai, X. Fan, Surface-functionalized nanoparticles as efficient tools in targeted therapy of pregnancy complications, Int. J. Mol. Sci. 20 (15) (2019).
[70] S.K. Kloet, A.P. Walczak, J. Louisse, et al., Translocation of positively and negatively charged polystyrene nanoparticles in an in vitro placental model, Toxicol. in Vitro 29 (7) (2015) 1701–1710.
[71] B. Ouyang, W. Poon, Y.N. Zhang, et al., The dose threshold for nanoparticle tumour delivery, Nat. Mater. 19 (12) (2020) 1362–1371.
[72] B.L. Mui, Y.K. Tam, M. Jayaraman, et al., Influence of polyethylene glycol lipid desorption rates on pharmacokinetics and pharmacodynamics of siRNA lipid nanoparticles, Mol. Ther. Nucl. Acids 2 (12) (2013) e139.
[73] H.I. Labouta, C. Sarsons, J. Kennard, et al., Understanding and improving assays for cytotoxicity of nanoparticles: what really matters? RSC Adv. 8 (41) (2018) 23027–23039.
[74] H.I. Labouta, T. Kraus, L.K. El-Khordagui, M. Schneider, Combined multiphoton imaging-pixel analysis for semiquantitation of skin penetration of gold nanoparticles, Int. J. Pharm. 413 (1–2) (2011) 279–282.
[75] R.E. Young, K.M. Nelson, S.I. Hofbauer, et al., Systematic development of ionizable lipid nanoparticles for placental mRNA delivery using a design of experiments approach, Bioact. Mater. 34 (2024) 125–137.
[76] H.C. Safford, K.L. Swingle, H.C. Geisler, et al., Orthogonal design of experiments for engineering of lipid nanoparticles for mRNA delivery to the placenta, Small 20 (41) (2023) e2303568.
[77] K.L. Swingle, M.M. Billingsley, S.K. Bose, et al., Amniotic fluid stabilized lipid nanoparticles for in utero intra-amniotic mRNA delivery, J. Control. Release 341 (2022) 616–633.
[78] Y. Zhu, R. Shen, I. Vuong, et al., Multi-step screening of DNA/lipid nanoparticles and co-delivery with siRNA to enhance and prolong gene expression, Nat. Commun. 13 (1) (2022) 4282.
[79] N. Chaudhary, A.N. Newby, M.L. Arral, et al., Lipid nanoparticle structure and delivery route during pregnancy dictate mRNA potency, immunogenicity, and maternal and fetal outcomes, Proc. Natl. Acad. Sci. USA 121 (11) (2024) e2307810121.
[80] B. Dugershaw-Kurzer, J. Bossart, M. Buljan, et al., Nanoparticles dysregulate the human placental secretome with consequences on angiogenesis and vascularization, Adv. Sci. (Weinh) 11 (28) (2024) e2401060.
[81] R.S. Riley, M.V. Kashyap, M.M. Billingsley, et al., Ionizable lipid nanoparticles for in utero mRNA delivery, Sci. Adv. 7 (3) (2021).
[82] M. Brentnall, L. Rodriguez-Menocal, R.L. De Guevara, E. Cepero, L.H. Boise, Caspase-9, caspase-3 and caspase-7 have distinct roles during intrinsic apoptosis, BMC Cell Biol. 14 (2013) 32.
[83] S. Cui, Y. Wang, Y. Gong, et al., Correlation of the cytotoxic effects of cationic lipids with their headgroups, Toxicol. Res. (Camb) 7 (3) (2018) 473–479.